Monthly Notices
of the
ROYAL ASTRONOMICAL SOCIETY

MNRAS **481,** 4940–4959 (2018)
Advance Access publication 2018 September 21

doi:10.1093/mnras/sty2576

The CGM and IGM at $z \sim 5$: metal budget and physical connection

Alex Codoreanu,[1,2,3]★ Emma V. Ryan-Weber,[1,2] Luz Ángela García,[1,2,4] Neil H. M. Crighton,[1] George Becker,[5] Max Pettini,[6] Piero Madau,[7] and Bram Venemans[8]

[1]*Centre for Astrophysics and Supercomputing, Swinburne University of Technology, Hawthorn, Victoria 3122, Australia*
[2]*ARC Centre of Excellence for All-sky Astrophysics (CAASTRO), Hawthorn, Victoria 3122, Australia*
[3]*Centre for Transformative Innovation, Hawthorn, Victoria 3122, Australia*
[4]*Universidad ECCI, Carrera 19 No. 49-20, Bogotá, Colombia*
[5]*Department of Physics Astronomy, University of California, Riverside, 900 University Avenue, Riverside, CA 92521, USA*
[6]*Institute of Astronomy, Madingley Road, Cambridge, CB3 0HA, UK*
[7]*Department of Astronomy & Astrophysics, University of California, 1156 High Street, Santa Cruz, CA 95064, USA*
[8]*Max-Planck Institute for Astronomy, Königstuhl 17, D-69117 Heidelberg, Germany*

Accepted 2018 September 14. Received 2018 September 14; in original form 2018 January 5

ABSTRACT

We present further results of a survey for absorption line systems in the spectra of four high redshift quasars ($5.79 \leq z_{\rm em} \leq 6.13$) obtained with the ESO Very Large Telescope X-Shooter. We identify 36 C IV and 7 Si IV systems with a $\geq 5\sigma$ significance. The highest redshift C IV and Si IV absorbers identified in this work are at $z = 5.80738 \pm 0.00017$ and $z = 5.77495 \pm 0.00038$, respectively. We compute the comoving mass density of Si IV ($\Omega_{\rm Si\,IV}$) and find that it evolves from $\Omega_{\rm Si\,IV} = 4.3^{+2.1}_{-2.1} \times 10^{-9}$ at $\langle z \rangle = 5.05$ to $\Omega_{\rm Si\,IV} = 1.4^{+0.6}_{-0.4} \times 10^{-9}$ at $\langle z \rangle = 5.66$. We also measure $\Omega_{\rm C\,IV} = 1.6^{+0.4}_{-0.1} \times 10^{-8}$ at $\langle z \rangle = 4.77$ and $\Omega_{\rm C\,IV} = 3.4^{+1.6}_{-1.1} \times 10^{-9}$ at $\langle z \rangle = 5.66$. We classify our C IV absorber population by the presence of associated *low-* and/or *high-ionization* systems and compute their velocity width (Δv_{90}). We find that all C IV systems with $\Delta v_{90} > 200\,{\rm km\,s^{-1}}$ have associated *low-ionization* systems. We investigate two such systems separated by 550 physical kpc along a line of sight, and find it likely that they are both tracing a multiphase medium where hot and cold gas is mixing at the interface between the circumgalactic medium and intergalactic medium. We further discuss the Mg II systems presented in a previous work and we identify 5 Si II, 10 Al II, 12 Fe II, 1 C II, 7 Mg I, and 1 Ca II associated transitions. We compute the respective comoving mass densities in the redshift range 2–6, as allowed by the wavelength coverage.

Key words: quasars: absorption lines – quasars: general – galaxies: statistics.

1 INTRODUCTION

Absorption systems in the spectra of high redshift quasi-stelar objects (QSOs) present an opportunity to identify and study intervening metal-enriched clouds during the first billion years of evolution of the Universe. Unambigous detection of these clouds is provided by the presence of doublets with high oscillator strength, such as Mg II (Kacprzak & Churchill 2011; Kacprzak et al. 2011; Kacprzak, Churchill & Nielsen 2012; Matejek & Simcoe 2012; Kacprzak et al. 2013; Bosman et al. 2017; Codoreanu et al. 2017), Si IV (Songaila 2005; Boksenberg & Sargent 2015) as well as C IV (Ryan-Weber, Pettini & Madau 2006; Simcoe 2006; Becker, Rauch & Sargent 2009; Ryan-Weber et al. 2009; Simcoe et al. 2011; D'Odorico et al. 2013; Díaz et al. 2016). The rest frame ionization wavelength and oscillator strength of each transition identified in this work are presented in Table 1.

These absorption systems are generally categorized into *low-* and *high-ionization* systems. *Low-ionization* absorption systems (Mg II, Si II, Al II, O I, and others) trace low-temperature/high-density regions connected to the circumgalactic medium (CGM; e.g. Steidel et al. 2010; Churchill et al. 2013; Nielsen, Churchill & Kacprzak 2013b; Nielsen et al. 2013a; Nielsen et al. 2015, 2016) while *high-ionization* absorption systems (C IV, Si IV, and others) trace high-temperature/low-density regions generally associated with the intergalactic medium (IGM; e.g. Schaye et al. 2003; Aguirre et al. 2004; Schaye, Carswell & Kim 2007; D'Odorico et al. 2016; Finlator et al. 2016; Keating et al. 2016; García et al. 2017; Oppenheimer et al. 2017).

However, such associations and boundaries are not always applicable as C IV systems with column densities $\log(N/{\rm cm}^2) > 13.5$ have also been associated with the haloes of galaxies with stellar

★ E-mail: acodoreanu@swin.edu.au

Table 1. Rest frame ionization wavelength (λ) and oscillator strength (*f*) of the ions identified in this work as reported in Morton (2003).

Ion	λ (Å)	*f*
C IV	1548.2049	0.189900
	1550.77845	0.094750
Si IV	1393.76018	0.513
	1402.77291	0.254
Mg II	2796.3542699	0.6155
	2803.5314853	0.3058
Mg I	2852.96328	1.830000
Al II	1670.7886	1.740
Si II	1526.70698	0.13300
	1260.4221	1.180
C II	1334.5323	0.127800
Fe II	2600.1724835	0.2394
	2586.6495659	0.069125
	2382.7641781	0.320
	2344.2129601	0.1142
	1608.45085	0.0577

mass (M_*) > $10^{9.5}$ $M_\odot$ at 0.0015 < z < 0.015 (Burchett et al. 2016). Furthermore, Steidel et al. (2010) and Turner et al. (2014) identify and measure the optical depth of C IV systems and find that they are preferentially found at a proper transverse distance of less than 200 kpc of $z \simeq$ 2–3 galaxies. Adelberger et al. (2005) also connects C IV systems with column densities log(N/cm^2) > 14.0 to young star-forming field galaxies up to $z \approx 3.3$ and finds that their gas halo can extend up to 80 kpc. Thus, *high-ionization* systems can also be found in virialized haloes where they are physically mixed with *low-ionization* systems.

Replicating the observed abundance and evolution of absorption systems beyond redshift 5 is a challenging task as they trace different physical environments and are sensitive to a large number of connected and correlated physical processes. For example, the galaxy contribution to the shape and amplitude of the global UV background (UVB; Oppenheimer, Davé & Finlator 2009) beyond redshift 5 depends on both the volume density of galaxies (Atek et al. 2015; Mason, Trenti & Treu 2015; Livermore, Finkelstein & Lotz 2017; Bouwens et al. 2015, 2017) and the properties of both PopII stars and the first metal-free stars (PopIII; i.e. Heger & Woosley 2002; Yoshida et al. 2006; Hosokawa et al. 2012; Pallottini et al. 2014). The relative abundance patterns described in Becker et al. (2012) are consistent with a scenario in which metal production in PopII stars dominates the metal budget by $z \sim 6$ but, currently, there is no clear observational tracer to signal the transition from PopIII to PopII stars which is expected to occur before $z \sim 10$ (Maio et al. 2010).

Furthermore, absorption systems are also sensitive to the yield and return fraction of metals (Madau & Dickinson 2014), which itself depends on both the initial mass function (Salpeter 1955; Kroupa 2001; Chabrier 2003) and the outflow models which transport those metals from the interstellar medium (ISM) to the IGM through the CGM (Ferrara, Pettini & Shchekinov 2000; Madau, Ferrara & Rees 2001; Oppenheimer & Davé 2006). Absorption systems are then an important observational discriminant as they trace diverse temperature and density regions and provide a census of metals (Lan & Fukugita 2017), which is not limited by the brightness of the galaxies associated with the enrichment.

Recent works by Bosman et al. (2017, hereafter B17) and Codoreanu et al. (2017, hereafter C17) have identified a population of *weak* Mg II systems (W_{2796}[1] ≤ 0.3 Å) from redshift 5 to 7. Previous works by Becker et al. (2006, 2011) have also identified *low-ionization* absorbers with multiple associated transitions (eg. O I, Si II, C II) beyond redshift 5. Their high incidence rates suggest that they are most likely tracing the small and numerous galaxies needed to reionize the Universe during the Epoch of Reionization (EoR) with $M_{\rm UV} \leq -13$ (Robertson et al. 2013). While these absorbers have not yet directly been connected to specific stellar populations, their presence indicates that metals, as traced by *low-ionization* systems, have already been well established and have a significant cross-section by redshift ∼6.

While these *weak* Mg II systems have a significant cross-section, they do not account for a large fraction of the metal budget. C17 have shown that Mg II systems with $W_{2796} \leq 1$ Å hold a small fraction (∼1/50) of the comoving mass density of Mg II ($\Omega_{\rm Mg\,II}$) in the redshift range $4.03 < z \leq 5.45$. Interestingly, C17 have also shown that $\Omega_{\rm Mg\,II}$, as measured by all systems discovered in their work,[2] increases from $\Omega_{\rm Mg\,II} = 2.1^{+6.3}_{-0.6} \times 10^{-8}$ at $\langle z \rangle = 2.48$ to $\Omega_{\rm Mg\,II} = 3.9^{+7.1}_{-2.4} \times 10^{-7}$ at $\langle z \rangle = 4.77$.

This order of magnitude increase is in contrast to the evolution of the comoving mass density of C IV ($\Omega_{\rm C\,IV}$) which has a flat evolution across a similar redshift range (Songaila 2001; Pettini et al. 2003). For example, Boksenberg & Sargent (2015, hereafter B15) measure a mean $< \Omega_{\rm C\,IV} > = 1.23 \pm 0.66 \times 10^{-8}$ at a mean redshift $\langle z \rangle = 3.20$ across the redshift range 1.9 < z < 4.5 and D'Odorico et al. (2013) measure $\Omega_{\rm C\,IV} = 1.4 \pm 0.3 \times 10^{-8}$ at $z = 4.818$. However, from redshift 5 to 6, $\Omega_{\rm C\,IV}$ declines by a factor of 2 to 4 (Simcoe 2006; Ryan-Weber et al. 2006; Becker et al. 2009; Ryan-Weber et al. 2009; Simcoe et al. 2011; D'Odorico et al. 2013).

The evolution in $\Omega_{\rm C\,IV}$ can be driven either by a change in the ionization state, the enrichment of the IGM (Becker, Bolton & Lidz 2015a) or both. It is reproduced in simulations by Oppenheimer & Davé (2006), Oppenheimer et al. (2009), Cen & Chisari (2011), and García et al. (2017). However, the opposite evolution of $\Omega_{\rm Mg\,II}$ when compared to the evolution of $\Omega_{\rm C\,IV}$ does not support an increase in the metal budget as the primary driver in the evolution of $\Omega_{\rm C\,IV}$ (C17). This suggests that the evolution of $\Omega_{\rm C\,IV}$ is then mostly driven by a change in the ionization state of the IGM resulting from changes in the UVB beyond redshift 5.

Finlator et al. (2016) investigate the impact of three different UVB prescriptions on the resulting absorber population and compare to the observational results of Becker et al. (2011) and D'Odorico et al. (2013, hereafter D13). The three types of UVBs tested are (1) the UVB presented by Haardt & Madau (2012, hereafter HM12), (2) a modified and directly simulated version of the HM12 UVB which accounts for inhomogeneous galaxy emissivity combined with a QSO emissivity, and (3) a QSO emissivity only. They find that while all three UVB scenarios can reproduce the column density distribution functions (CDDFs) of C II, Si IV, and C IV only (2) reproduces the observed ionic ratios of Si IV/C IV and C II/C IV.

Interestingly, the QSO-only UVB model greatly overproduces photons with energies greater than 4 Ryd which is reflected in an over production of C IV (4.7 Ryd). However, at lower energies, probed by Si IV, Si II, and C II, all three UVB models have similar intensities. Thus, simply scaling up the intensity of the UVB would result in different ratios of Si IV/C IV and C II/C IV than a UVB which is adjusted by considering varying contributions from sources of harder photons such as QSOs or PopIII stars (Finlator et al.

[1]The equivalent width of the Mg II λ2796 transition.
[2]$0.117 \leq W_{2796} \leq 3.655$ Å

2016). Recently, Doughty et al. (2018) have also shown that aligned absorber pairs (e.g. multiple ions associated with the same enriched and ionized gas halo) can be used to improve the constraints on the UVB. They found that the observed statistics of C IV/Si IV are best reproduced by a hard, spatially uniform UVB but, a single aligned Si II/Si IV pair is reproduced best by the HM12 UVB prescription.

Thus, understanding the evolution of both *low-* and *high-ionization* systems is then necessary as *low-ionization* systems (i.e. C II, Si II) are sensitive to both changes in ionization and gas density/metallicity (Finlator et al. 2015) while C IV is mostly sensitive to ionization prescriptions (Finlator et al. 2016). Future simulations can explore if there is a preferred balance between changes to a global UVB from local sources in conjunction with different prescriptions for self-shielded haloes which produce metals but do not contribute photons to the global UVB. In order to test such scenarios several questions arise:

(i) 'How does $\Omega_{\rm Si\,IV}$ evolve beyond redshift 5?'
(ii) 'What is the physical connection between *low-* and *high-ionization* systems beyond redshift 5?'
(iii) 'Are *low- and high-ionization* systems tracing distinct physical constructs or are they tracing multiphase gas at virial distances or at the interface between the CGM and IGM?'
(iv) 'What is the evolution of other species of *low-ionization* systems (i.e. Si II, C II, Fe II, and others)?'

We explore these questions by searching for intervening absorption systems in four medium resolution and signal-to-noise spectra of redshift ∼6 QSOs. These spectra were investigated for the presence of Mg II systems and the results were presented in C17. In this work, we provide the first $\Omega_{\rm Si\,IV}$ values and corresponding CDDFs beyond redshift 5. We compare with C IV in the range $4.92 < z < 6.12$. We also identify Si II, Al II, Fe II, C II, Mg I, and Ca II associated transitions in addition to the Mg II discussed in C17. We discuss the details of the identification of all absorption systems in Section 2. We discuss our treatment of false positive contamination and completeness considerations in Section 3. We provide the incidence rates, comoving mass densities, and CDDFs (and best-fitting parameters) of the Si IV and C IV systems identified in this work in Section 4. We present the comoving mass densities of Mg I, Ca II, Si II, Al II, Fe II, and C II and discuss our results in Section 5. We provide a summary and conclusions in Section 6. Throughout this paper we use a ΛCDM cosmology with $\Omega_{\rm M} = 0.308$ and $H_0 = 67.8\,{\rm km\,s^{-1}\,Mpc^{-1}}$ (Planck Collaboration 2015).

2 CANDIDATE SELECTION

The observations, exposure times, data reduction, and instrument resolution are described in C17. The reduced spectra are binned with a resolution of $10\,{\rm km\,s^{-1}}$ pixel^{-1}. We follow the same steps as C17 in identifying absorbers and quantifying the completeness of our survey. In short, we first create a candidate list using an automatic search algorithm whose output is then visually inspected by the lead author (AC) and a final list of candidates is created. These candidate absorbers are then fit with Voigt profiles using VPFIT 10.0 (Carswell & Webb 2014).

2.1 Automatic search

In order to identify C IV and Si IV doublets, we create a candidate list by finding all pixels of the spectra which meet the following conditions:

(i) a minimum three consecutive $5\sigma_i$ pixel detections;

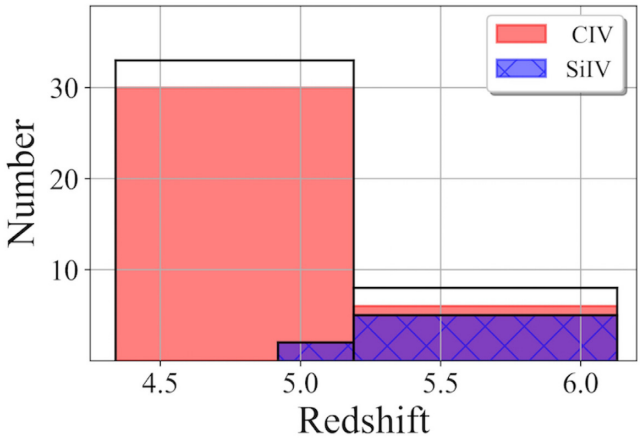

Figure 1. Histograms of C IV and Si IV discovered systems. The raw counts are denoted by black outlines while the number of systems which pass the 5σ recovery selection criteria are shaded in red and cross-hatched blue, respectively. All values are presented in Table 2.

$\sigma{\rm i} = \frac{(1-F_\lambda i)}{E_\lambda}$
(ii) $W_{\rm d1}/\sigma\,W_{\rm d1} \geq 5$ or $W_{\rm d2}/\sigma\,W_{\rm d2} \geq 5$
(iii) $0.5 \leq (W_{\rm d1} \pm \sigma\,W_{\rm d1})/(W_{\rm d2} \pm \sigma\,W_{\rm d2}) \leq 5$, searching for C IV
(iv) $0.8 \leq (W_{\rm d1} \pm \sigma\,W_{\rm d1})/(W_{\rm d2} \pm \sigma\,W_{\rm d2}) \leq 4$, searching for Si IV,

where $F_\lambda i$ and $E_\lambda i$ are the flux and error values associated with a pixel i. W and σW represent the equivalent width and error of the consecutive pixels associated with the C IV λλ1548 1550 and Si IV λλ1393 1402 doublet candidates where d1 and d2 denote each one of the respective transitions. The respective equivalent width ratios[3] are chosen by the lead author in order to minimize the contamination by false positives. These ratios represent only the pixel flux and error values and do not account for possible blends with other transitions. The selection algorithm outputs 94 candidate C IV systems (with 118 components) and 18 candidate Si IV systems (with 40 components).

2.2 Visual check

Each candidate is visually inspected by the lead author (AC) and selected as an absorber based on the similarity of the velocity profile of the two transitions in each doublet. In C17, most of the rejected Mg II candidates occurred in the NIR where telluric absorption and sky-line emissions heavily polluted the spectra. In the present work, the majority of the absorption path – redward of the Ly α emission peak of the QSO to within $3000\,{\rm km\,s^{-1}}$ of the QSO redshift – for C IV and Si IV is in the VIS arm of X-Shooter.

The rejected candidates have mis-matched velocity profiles or are weak features dominated by rms fluctuations. From the 94 C IV candidates, 41 are accepted and from the 18 Si IV candidates, 7 are accepted by the lead author as possible 'true' absorbers (see Fig. 1 and $\bar{N}$ column in Table 2). Following this selection, we search for associated ions (C II, Si II, Mg I, Al II, Al III, N V, O I, O VI, Fe II, and Ca II) by using the C IV, Si IV, and Mg II (described in detail in C17) doublets as redshift anchors for their possible location. For this task, we use the PLOTSPEC package.[4]

[3] $(W_{d1} \pm \sigma\,W_{d1})/(W_{d2} \pm \sigma\,W_{d2})$.
[4] Developed by Dr. Neil Crighton https://github.com/nhmc/plotspec/

Table 2. Median redshift values ($\langle z \rangle$), redshift bins (Δz), number of discovered systems ($\bar{N}$), number of recovery selected systems ($\ddot{N}$), adjustment scalars (A), redshift path (dz), comoving absorption path (dX), incidence rates (dN/dz), comoving incidence rates (dN/dX), and comoving mass densities (Ω) for C IV and Si IV.

Ion	$\langle z \rangle$	Δz	$\bar{N}$	$\ddot{N}$	A	dz	dX	dN/dz	dN/dX	Ω
C IV	4.77	4.33–5.19	33	30	1.47	2.86	12.37	15.4 ± 2.8	3.6 ± 0.6	$1.6^{+0.4}_{-0.1} \times 10^{-8}$
	5.66	5.19–6.13	8	6	2.29	3.13	14.42	4.4 ± 1.2	0.9 ± 0.3	$3.4^{+1.6}_{-1.1} \times 10^{-9}$
Si IV	5.05	4.92–5.19	2	2	2.12	0.43	1.98	9.8 ± 4.7	2.2 ± 1.1	$4.3^{+2.1}_{-2.1} \times 10^{-9}$
	5.66	5.19–6.13	5	5	1.49	3.13	14.42	2.4 ± 0.9	0.5 ± 0.2	$1.4^{+0.6}_{-0.4} \times 10^{-9}$

We find 12 systems with multiple associated ions and each one is discussed in Section 2.4. The C IV associated with system 9 in sightline *ULAS J*1319 + 0959 does not meet our 5σ discovery criteria (see Section 2.1) but is included in our analysis for reasons discussed in Section 2.4.4. It is the only absorber 'manually' introduced. The rejected systems are single component systems and have no other associated transitions (ie. Fe II, C II). Thus, we are not forced to consider multiple ions when trying to ascertain the veracity of an absorption system.

2.3 Voigt profiles and equivalent widths

We use VPFIT 10.0 to fit Voigt profiles to the absorption lines and we do not tie associated transitions together as they could trace multiphase gas. However, Boksenberg & Sargent (2015) allow the fixed gas temperature to vary in the range $10^4 < T < 10^5$ K and has shown that the VPFIT retrieved column density parameters of Voigt profiles do not depend strongly on the temperature. For reference, the thermally broadened profile of a 10^5K g as cloud results in an upper bound for the thermal broadening parameter of $b_{\rm therm} \simeq 10\,{\rm km\,s^{-1}}$. As recommended in Carswell & Webb (2014), we impose a minimum $b << b_{\rm expected}$. We choose a minimum value of $b = 1\,{\rm km\,s^{-1}}$.

As the dominant source of uncertainty arises from the continuum fitting process, we adjust the continuum level by ±5 per cent and repeat the entire fitting procedure. This leads to the error bars associated with each set of Voigt profile parameters. The redshift (z) and Doppler parameter (b) of each absorber is fit individually and no absorbers reported in this work are highly saturated.

A system is defined as all components within $0 \leq \Delta v^5 \leq 500\,{\rm km\,s^{-1}}$. We select this Δv width range to account for the possible stellar velocity dispersion of galaxies with an intrinsic B-band magnitude $M_B \geq -25$ (Faber & Jackson 1976) as we have no a priori information on the associated galaxies. The velocity width of a system (Δv_{90}) is then computed from the corresponding wavelength boundary ($\Delta\lambda$; Prochaska et al. 2008) enclosing 90 per cent of the optical depth of all components. We compute the equivalent width (W_0) of each component over each associated $\Delta\lambda$ value. The W_0 of blended systems is computed from the Voigt profile fit. The total column density of an absorption system is computed by summing the column densities of the components.

We present all identified systems, their components, equivalent width, Voigt profile parameters, associated errors, and recovery levels in the system tables available in the online appendix. All visually selected systems (see Section 2.2) from the automated output created by the detection algorithm (see Section 2.1) are discussed in the following section.

2.4 Individual sight lines

The four QSO redshifts, apparent magnitudes, and initial discoveries are described in C17. We observed each object for ∼10 h. Below, we present all C IV and Si IV absorbers along with associated transitions. Given that all Mg II absorbers have been presented in C17, we only include them in the system plots available in the online appendix (see Fig. 2 for an example). No additional Mg II absorbers are found after identifying the C IV and Si IV doublets. Blended components are marked with a ⇓ while those polluted by a sky-line or poor subtraction residual are marked with a ⇑. Systems which do not meet the 5σ recovery selection criteria in their respective (log(N), dz_j) bins are identified with a^*. We discuss this in detail in the follow-up Section 3.

Additionally, we present, in the online appendix, the associated transitions (Mg I, Fe II, Al II, and Ca II) of Mg II discoveries from C17 with redshifts outside this paper's search region defined by the C IV and Si IV wavelengths. For ease of understanding to those reading the following subsections in detail, we recommend to have the online appendix at hand. We only include Fig. 2 and Table 3 in the main paper as an example.

2.4.1 ULAS J0148+0600

We present nine new systems and the highest redshift absorber in this sightline which meets our 5σ recovery selection criteria is system 9 with $z = 5.82630 \pm 0.00013$. All systems and associated components are presented in detail in section A of the online appendix.

Systems 1, 5, 7 are single component C IV systems. System 9 is a single Si IV system with both the λλ1393 1402 features blended with the C IV λ1550 feature of system 7 and a Fe II λ2382 absorber at $z \simeq 3.01858$, respectively. Furthermore, the Si IV λ1393 could also be a Mg II λ2796 system at $z \simeq 2.4024$. This possible Mg II system is not chosen from the initial candidate list by the lead author due to relative velocity structure of the λ2796 and λ2803 features.This system is of particular interest as it falls in the redshift range $5.523 < z < 5.879$ which corresponds to a large Lyα trough discussed in detail by Becker et al. (2015b). This is one of two possible metal absorption systems in the corresponding redshift range. However, there are no other absorbers associated with this Si IV system and both transitions are heavily blended. Is this then a real system?

We find that this is the only Si IV system with no other associated absorbers such as C IV, Si II, or Fe II. All other Si IV systems identified in this work as well as those of B15[6] and D13 have at least

[5] $\Delta v = c \times \Delta\lambda$, where c is the speed of light.

[6] See their Tables 2-10.

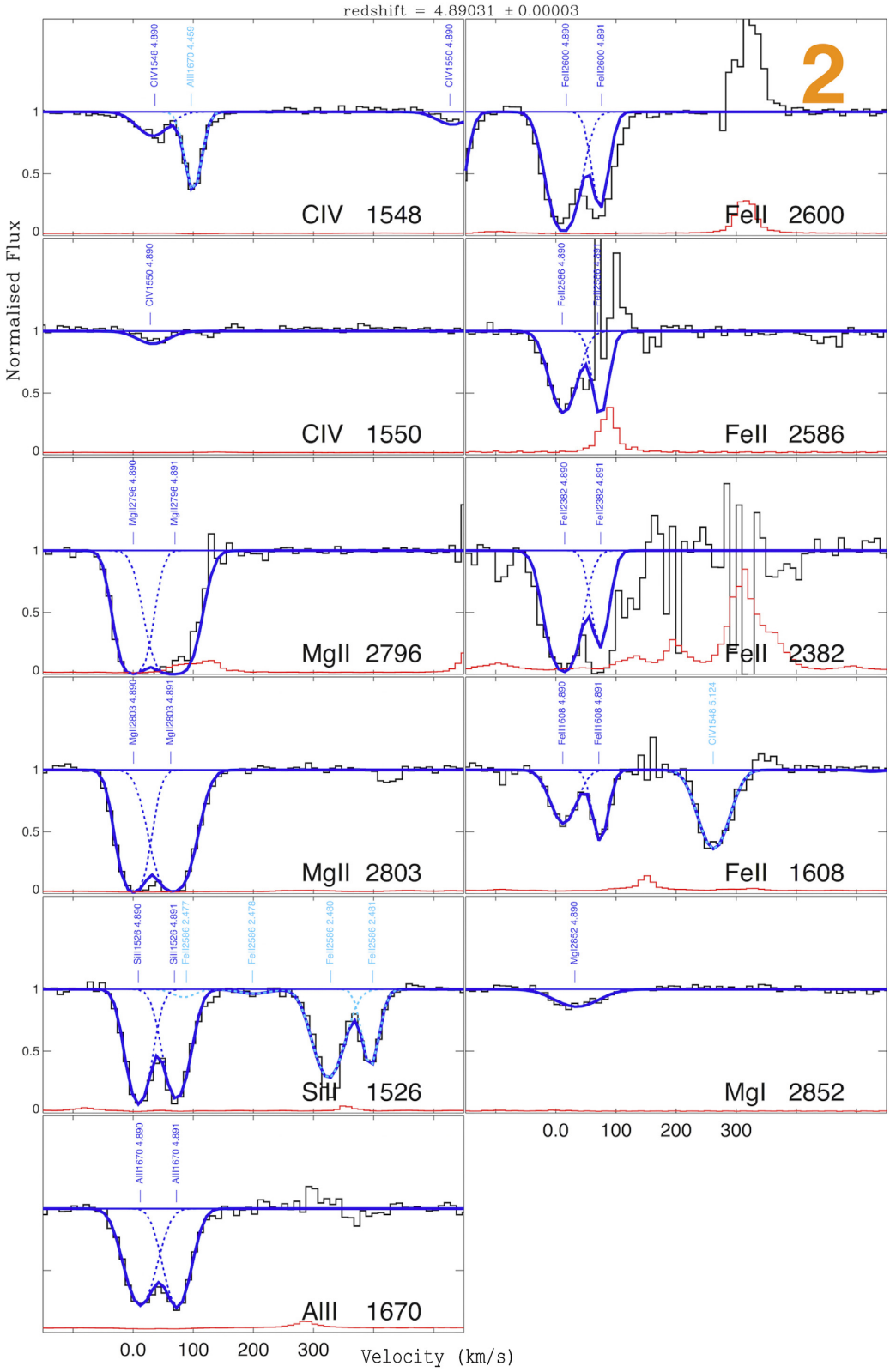

Figure 2. System 2 identified in the ULAS J0148+0600 sightline. Each transition is identified in the bottom right of each panel. In each panel, the vertical axis is the continuum normalized flux. The horizontal axis is the velocity separation (km s^{-1}) from the lowest redshift component of a system. The normalized spectrum is plotted in black and the associated error is in red. The solid blue line represents the full fit to the spectra and includes other ions besides the transition identified in the bottom right of each panel. Individual components are plotted with dashed lines and are identified by a vertical label. The identified transition components are in solid blue and other transitions are in light blue.

Table 3. Absorption systems identified in ULAS J0148+0600 sightline. A system is defined as all components within 500 km s^{-1} of the lowest redshift component. Each component is marked with a letter id and all associated transitions are identified in the ion column. The table also lists z, W_0, log(N), and b which are the redshift, equivalent width, column density, and doppler parameter for each component Voigt profile fit. The 5σ recovery selection criteria are defined in equation (7). No lower bound is presented for systems with $b = 1$ km s^{-1} as the minimum doppler parameter we allow for a Voigt profile is 1 km s^{-1}.

Sys	ID	Ion	ULAS J0148+0600 z	W_0 (Å)	log(N/cm^2)	b (km s^{-1})	5σ recovery rate
1	a	CIV 1548	$4.57120 \pm 9.0 \times 10^{-5}$	0.042 ± 0.002	$13.06^{+0.45}_{-0.26}$	$25.0^{+64.1}_{-6.77}$	0.93
		CIV 1550		0.020 ± 0.001			
2	a	CIV 1548⇓	4.89095 ± 0.00015	0.059 ± 0.002	$13.24^{+0.38}_{-0.16}$	$31.8^{+67.6}_{-4.46}$	0.96
		CIV 1550		0.031 ± 0.003			
		MgI 2852	$4.89099 \pm 6.8 \times 10^{-5}$	0.121 ± 0.006	$11.98^{+0.27}_{-0.20}$	$47.7^{+22.1}_{-8.96}$	
		SiII 1526⇓	$4.89049 \pm 3.7 \times 10^{-5}$	0.233 ± 0.002	$14.43^{+0.15}_{-0.08}$	$17.8^{+0.48}_{-1.24}$	
		AlII 1670	4.89054 ± 0.00013	0.268 ± 0.004	$13.05^{+0.06}_{-0.06}$	$27.3^{+1.42}_{-1.92}$	
		FeII 2600	$4.89056 \pm 7.5 \times 10^{-5}$	0.522 ± 0.004	$14.07^{+0.09}_{-0.08}$	$23.7^{+3.84}_{-1.82}$	
		FeII 2586⇑		0.307 ± 0.008			
		FeII 2382⇑		0.551 ± 0.011			
		FeII 1608		0.110 ± 0.003			
	b	SiII 1526	$4.89172 \pm 4.3 \times 10^{-5}$	0.223 ± 0.002	$14.30^{+0.07}_{-0.06}$	$20.0^{+0.67}_{-1.54}$	
		AlII 1670	4.89175 ± 0.00012	0.243 ± 0.005	$13.02^{+0.06}_{-0.06}$	$22.5^{+1.53}_{-2.13}$	
		FeII 2600	$4.89176 \pm 5.7 \times 10^{-5}$	0.208 ± 0.003	$14.30^{+0.53}_{-0.08}$	$7.04^{+1.65}_{-0.17}$	
		FeII 2586		0.181 ± 0.044			
		FeII 2382		0.223 ± 0.010			
		FeII 1608		0.096 ± 0.003			
3	a	CIV 1548	4.93212 ± 0.00011	0.093 ± 0.002	$13.48^{+0.00}_{-0.10}$	$18.7^{+5.74}_{-3.79}$	0.97
		CIV 1550		0.052 ± 0.002			
	b	CIV 1548	4.93308 ± 0.00020	0.057 ± 0.002	$13.22^{+0.07}_{-0.16}$	$20.8^{+9.50}_{-3.77}$	0.96
		CIV 1550		0.029 ± 0.002			
	c	CIV 1548	4.93463 ± 0.00030	0.042 ± 0.003	$13.07^{+0.25}_{-0.27}$	$38.3^{+8.97}_{-10.1}$	0.95
		CIV 1550		0.022 ± 0.003			
4	a	CIV 1548	4.95183 ± 0.00033	0.013 ± 0.002	$12.56^{+0.73}_{-0.69}$	$19.2^{+66.5}_{-18.2}$	0.71
		CIV 1550		0.006 ± 0.002			
	b	CIV 1548	4.95809 ± 0.00027	0.012 ± 0.002	$12.56^{+0.68}_{-0.42}$	$3.58^{+77.6}_{-2.48}$	0.71
		CIV 1550		0.006 ± 0.002			
5	a	CIV 1548	5.02327 ± 0.00013	0.092 ± 0.010	$13.49^{+0.13}_{-0.11}$	$16.1^{+7.78}_{-5.47}$	0.93
		CIV 1550		0.052 ± 0.008			
6	a	CIV 1548	$5.12488 \pm 6.9 \times 10^{-5}$	0.199 ± 0.005	$13.87^{+0.07}_{-0.07}$	$28.0^{+0.61}_{-2.04}$	0.97
		CIV 1550⇓		0.119 ± 0.004			
		SiIV 1393	$5.12509 \pm 6.7 \times 10^{-5}$	0.040 ± 0.001	$12.75^{+0.26}_{-0.21}$	$24.3^{+15.7}_{-5.55}$	0.96
		SiIV 1402		0.022 ± 0.001			
7	a	CIV 1548⇓	5.13495 ± 0.00024	0.076 ± 0.005	$13.33^{+0.20}_{-0.18}$	$35.1^{+30.2}_{-8.21}$	0.94
		CIV 1550⇓		0.036 ± 0.003			
8	a	SiIV 1393	5.77495 ± 0.00038	0.029 ± 0.013	$12.63^{+0.21}_{-0.22}$	$6.54^{+7.25}_{-5.42}$	0.64
		SiIV 1402		0.016 ± 0.005			
		SiII 1260	$5.77515 \pm 8.5 \times 10^{-5}$	0.003 ± 0.006	$12.23^{+0.20}_{-0.20}$	$13.7^{+6.36}_{-7.97}$	
9	a	SiIV 1393⇓	5.82630 ± 0.00013	0.035 ± 0.002	$12.71^{+0.14}_{-0.12}$	$9.70^{+3.12}_{-6.98}$	0.68
		SiIV 1402⇓		0.019 ± 0.001			

⇓ denotes a component with a blended feature.
⇑ denotes a component polluted by a sky-line or poor subtraction residual.
* denotes system which does not meet our 5σ recovery selection criteria.

one other associated absorber. Given this extra information, we suspect that this individual Si IV absorber is a false positive. However, since we do not use such criteria for the selection of other absorbers and this system does meet our general selection criteria described in Sections 2.1 and 2.2, we include it in the absorber population statistics. These statistics are adjusted for *user success/failure, false positive contamination* and *completeness* as described in Section 3.

The second system in the redshift range $5.523 < z < 5.879$ is system 8, a single component absorber anchored by Si IV with associated Si IIλ1260. We note that System 8 is a marginal detection as both transitions are affected by skyline residuals. The presence of the associated Si II λ1260 lends credibility to the detection but, itself, was identified as a possible Mg II doublet by the automatic detection algorithm. It was not selected by the lead author as the $\lambda\lambda$2796 2803 transitions were not well matched when considering the full absorption profile composed of the Si II λ1260 component of System 8 and the Si IV λ1393 component of system 6.

System 2 is anchored by C IV (C IV λ1548 blended with Al II $\simeq 4.45996$) and Mg II doublets. We identify associated Fe II (Fe II λ2585 blended with a skyline), Mg I, Si II (blended with Fe II at $z \simeq 2.47759$), and Al II. System 3 is a three component C IV system. System 4 is a two component C IV system. System 6 is a two

component system with C IV and Si IV absorbers. System 7 is a C IV absorber whose λ1548 feature is blended with the C IV λ1550 feature of system 6.

2.4.2 SDSS J0927+2001

We present 10 new systems and the highest redshift absorber in this sightline which meets our 5σ recovery selection criteria is system 10 with $z = 5.66382 \pm 0.00020$. All systems and associated components are presented in detail in section B of the online appendix.

Systems 1, 2*, 3, 6, 7, and 9 are single component C IV systems. Systems 4 and 10 are two component C IV systems. System 5 is a 3 component C IV system where the third component has associated Al IIλ1670 which is heavily blended with a Mg II system with $z = 2.34879 \pm 1 \times 10^{-5}$. System 5 also has an associated Mg II absorber. System 8 is a single component system with both C IV and Si IV absorbers.

2.4.3 SDSS J1306+0356

This sightline was previously investigated by D13, who confirm systems 2, 4, 8, and 9 first identified by Simcoe et al. (2011, hereafter S11). D13 first discover systems 1, 3, 5, and 6. The highest redshift absorber in this sightline which meets our 5σ recovery selection criteria is system 15 with $z = 5.80738 \pm 0.00017$. All systems and associated components are presented in detail in Section C of the online appendix.

We present seven new systems 7, 10, 11*, 12, 13*, 14*, and 15 with four of them passing our 5σ recovery selection criteria. Systems 5, 6, 7, 10, 11*, 12, 13*, 14*, and 15 are single component C IV systems. Systems 1 (C IV λ1550 blended with the Si IIλ1526 feature of system 2), 3 and 4 are two component C IV systems.

System 2 is a complex absorber anchored by C IV and Mg II doublets with associated Al II, Fe II, and Si II. We note that the Al IIλ1670 component *b* is most likely blended with an unidentified transition which results in an artificial broadened profile. This results from the fact that we do not tie the Doppler *b* parameter of the ionization systems during the Voigt profile fitting.

S11 suggest a possible C IV system at $z = 4.702$ and it is flagged by the automatic detection algorithm (Section 2.1) but the λ1548 feature is contaminated by a sky-line while the possible λ1550 feature is actually the λ1548 feature of system 5. For these reasons, this candidate is rejected by the lead author in the visual inspection step (Section 2.2). During the same visual inspection step, the lead author also does not select system 2 presented by D13 ($z = 4.58040 \pm 7 \times 10^{-5}$) as the λ1550 feature is not well matched with the λ1548's velocity structure.

System 8 is a complex absorber anchored by C IV and Mg II doublets with associated Al II, Mg I, Fe II, and Si II as first suggested by S11. System 9 is a similarly complex absorber with much weaker Mg I which we were not able to fit confidently. The systems could not be fit when the continuum was adjusted by +0.05. These two systems were discussed in C17 as they prove challenging to the system definition (all components within 500 km s^{-1}) and system 9 is omitted by Chen et al. (2017) from their analysis. In order to highlight these systems, we plot them together in Fig. 18. We anchor the velocity scale on the bluest C IV component ($z = 4.85878 \pm 3.5 \times 10^{-5}$) and then plot vertical dashed lines at three 500 km s^{-1} intervals. As can be seen, the reddest component of system 8 is within 500 km s^{-1} of the bluest component of system 9 but each system has distinct velocity structures. We also plot vertical dashed lines at +600 and +900 km s^{-1} and we discuss these systems in more detail in Section 5.3.

2.4.4 ULAS J1319+0959

This sightline was previously investigated by D13, who confirm systems 6 and 9 first identified by S111 and first discover systems 1, 2, 3, 4, and 8. D13 treat our system 2 as two systems given that their distinct components are separated by ∼350 km s^{-1}. However, in order to be consistent with our definition of a system[7] we treat this as a single system. The highest redshift absorber in this sightline which meets our 5σ recovery selection criteria is system 9 with $z = 5.57037 \pm 0.00033$. All systems and associated components are presented in detail in Section D of the online appendix.

We present two new systems, 5 and 7*. We only use system 5 in our analysis as system 7 does not meet our 5σ recovery selection criteria. Systems 1, 2, 4, 5, and 7* are single component C IV systems. System 2 (C IV λ1550 of component *b* is blended with the C IV λ1548 components of system 3) is a two component C IV system.

System 3 is anchored by both C IV and Mg II. The C IV λ1548 features are blended with the C II component of system 9 and the C IV λ1550 of system 2. The C IV λ1550 features are blended with the Si IV λ1402 features of system 6. System 6 is a two component Si IV system where component *b* also has associated C IV. System 8 is a two component system anchored by C IV, Si IV, and Mg II. Component *b* also has associated Al IIλ1670.

System 9 is a three component system anchored by Si IV. The C IV associated with system 9 is not detected by the automatic detection algorithm at a 5σ cutoff but component *b* is detected at a 3σ selection. We introduce the absorber as it was previously discovered by S11 and D13 and has associated Si IV doublet to also anchor the redshift of the absorber. We discuss the impact of this decision on our resulting incidence line statistics (Section 4.1), comoving mass density calculation (Section 4.2), and resulting CDDFs (Section 4.3). We confirm the possible associated C II first suggested by S11 but we do not identify any associated Fe II. We do identify associated Al IIλ1670.

We are not able to confirm the D13 systems 2 ($z = 4.62931 \pm 8 \times 10^{-5}$) and 6 ($z = 4.70325 \pm 2 \times 10^{-5}$) as they are not flagged by our automatic detection algorithm and do not have other associated transitions to solidify the identification.

3 SURVEY COMPLETENESS AND FALSE POSITIVE CORRECTIONS

When considering the statistics of absorption line systems we must account for the wavelength dependent signal-to-noise profile (visual versus near-infrared) as well as the strength of the absorber (equivalent width or column density). Furthermore, one must account for the human impact if a visual inspection/user voting process selects from the output of an automatic detection algorithm. In summary, we use the prescriptions put forth in C17, which follow the steps described in Matejek & Simcoe (2012).

We first create a library of C IV and Si IV absorbers which are inserted at every Å in the spectra of each QSO. We then search for them using the same automatic detection algorithm described in Section 2.1. Following this, the lead author quantifies their ability to accurately identify true absorbers (*user success*) as well as incorrectly identify random features or artificially spaced doublets[8] as true absorbers (*user failure*). *User success* and *user failure* are computed as functions of S/N. We then turn these *user success* and *user failure* likelihoods into 2D maps with the same resolution

[7] All components within 500 km s^{-1}.
[8] Described in Section 3.3.

as the recovery grids outputted by the automatic detection algorithm. We combine these and create recovery maps adjusted for *user success/failure* for each sightline for both C IV and Si IV doublets.

In order to account for false positive contamination, we repeat the entire analysis and completeness calculations for the artificially spaced doublets: C IV′ (λλ1548.2049 1553.3519) and Si IV′ (λλ1393.76018 1411.78580). We then combine the results of this search and analysis of artificially spaced doublets with that of the true C IV and Si IV absorbers to compute a single scalar which accounts for variable completeness across a redshift bin, the strength of the absorber, false positive contamination as well as the impact of the human interaction step (see *A* in Table 2). We present the details of each step below.

3.1 Automatic recovery of doublets

In order to identify the true number of absorbers for a given redshift path, dz, we must first identify for what fraction of that path we can confidently identify the discovered absorbers. This recovery fraction is a function of both the strength of the absorber and the signal-to-noise profile of each quasar spectrum considered. As a first step, we use RDGEN (Carswell et al. 2014) to extract a library of Voigt profiles consistent with the observed components. For C IV, we extract absorbers with a column density range $12.5 \leq \log(N_{\rm sys}/{\rm cm}^2) \leq 14.5$ in 0.1 increments. For Si IV, we extract absorbers with a column density range $12.2 \leq \log(N_{\rm sys}/{\rm cm}^2) \leq 13.8$ in 0.1 increments. For each column density, we extract six profiles with a b parameter value in the range $10 \leq b \leq 60\,{\rm km\,s^{-1}}$ with a step size of $10\,{\rm km\,s^{-1}}$. We sample every Å where C IV or Si IV can be observed by injecting an absorption system in 100 Å steps. In total, we insert and search for 444 288 Si IV and 1078200 C IV absorbers.

The injected systems are searched for automatically using the same simple algorithm used to create the initial candidate lists described in Section 2.1. The output of the detection algorithm is a Heaviside function, $H(\log(N), b, z)$, where $\log(N_{\rm sys}/{\rm cm}^2)$, b, and z are the column density, Doppler parameter, and redshift location of the inserted C IV and Si IV Voigt profile. The values of the output are

$$H(\log(N, b, z) = \begin{cases} 0 & \text{if the injected system is not detected,} \\ 1 & \text{if the injected system is detected,} \end{cases} \quad (1)$$

Next, we bin the above Heaviside function across all b values and redshift bins ($dz = 0.01$) and compute the recovery fraction of an inserted doublet as

$$L(\log(N, dz_j) = \frac{1}{n}\sum_{i=1}^{n} H(\log(N), b, z), \quad (2)$$

where n is the total number of inserted systems such that $z \in {\rm d}z_j$ with column density $\log(N_{\rm sys}/{\rm cm}^2)$. This above expression denotes how often an inserted absorber would make it on to the initial candidate list which was then visually inspected by the lead author.

3.2 Adjusting for user interaction

In order to account for the ability of the lead author to accurately identify an absorber, we create a simple simulation which randomly chooses to/not to insert an absorber with/without a true rest-frame separation. This randomization ensures that there is no a priori expectation on whether an absorber is inserted and if so, if it is a true absorber. We will describe the *false* absorbers in the following Section (3.3). This voting process is run by eye for 12 000 instances. The results (1-for discovery, 0-no discovery) are binned as a function of the boxcar S/N of the inserted feature SNR $\equiv W_{\rm d1}/\sigma W_{\rm d1}$.[9]

Next, we fit the *user success* (using a χ^2 minimization technique) with an exponential function of the form

$$P_{d1}({\rm SNR}) = P_{\infty}(1 - e^{S/{\rm SNR}}), \quad (3)$$

where P_{∞} is the probability that the user will accept a true absorption system and S is an SNR exponential scale factor. Just as we found in C17 and similar to the findings of Matejek & Simcoe (2012) and Chen et al. (2017), we find that even for the best S/N regions, the user acceptance rate is not 100 per cent, except for the artificial doublet Si IV′.

Following this, we next fit the *user failure* with a triangle function

$$P^{\rm FP}({\rm SNR}) = \begin{cases} P^{\rm FP}_{\rm max}\left({\rm SNR}/s_p\right) & {\rm SNR} \leq s_{\rm p}, \\ P^{\rm FP}_{\rm max}\left(\frac{{\rm SNR}-s_f}{s_p-s_f}\right) & {\rm SNR} > s_{\rm p}, \end{cases} \quad (4)$$

where $P^{\rm FP}_{\rm max}$ is the maximum contamination rate which arises at $s_{\rm p}$. We find that the user acceptance of injected false doublets as real approaches 0 as the SNR reaches ∼13. The binned values and best fits can be seen in Fig. 3. All best-fitting values can be seen in Table 4.

Finally, we turn the *user success* and *user failure* functional values (equations 3 and 4) into grids binned with the same resolution as the recovery function (equation 2). The resulting grids are denoted as $A(\log(N), {\rm d}z_j)$ and $A^{\rm FP}(\log(N), {\rm d}z_j)$, respectively. Following this, we combine the recovery rate (from the automatic detection) with the *user success* grids

$$C(\log(N), dz_j) = L(\log(N), dz_j) \times A_{d1}(\log(N), dz_j) \quad (5)$$

and an example can be seen in (4). The recovery fraction corrected for *user success* associated with each doublet can be seen in the 5σ recovery rate columns of each sightline discovery table available in the online appendix (see Table 3 for an example). Thirty seven C IV systems and seven Si IV systems survive a 5σ cutoff. For our analysis, we only use those systems with at least one component with 5σ 50 per cent or greater recovery fraction corrected for *user success*, except for system 9 in *ULAS J*1319 + 0959 for reasons described in Section 2.4.4.

3.3 False positives

In order to quantify the contamination by false positive doublets, we search for the artificially spaced absorbers: C IV′(λλ1548 1553) and Si IV′(λλ1393 1411). We perform this investigation in the same fashion as the search for the C IV and Si IV doublets.

We first create an initial candidate list using the same detection algorithm described in Section 2.1. The automatic detection algorithm outputs 76 C IV′ and 32 Si IV′ candidates. The lead author then selects three C IV′ and one Si IV′ possible absorbers. These absorbers are selected for their similar velocity profile, with the same considerations described in Section 2.2. Following this, we adjust VPFIT to fit the above artificial doublets and measure their column density and Doppler parameter.

Next, we extract a library of artificial ions which we then insert and search for in the same manner and with the same resolution as described in Section 3.1. The results are then binned and adjusted for *user success* (see equation 5). The resulting maps can be seen

[9] $d1$ denotes the λ1548 or λ1393 feature of the C IV and Si IV true and false absorbers.

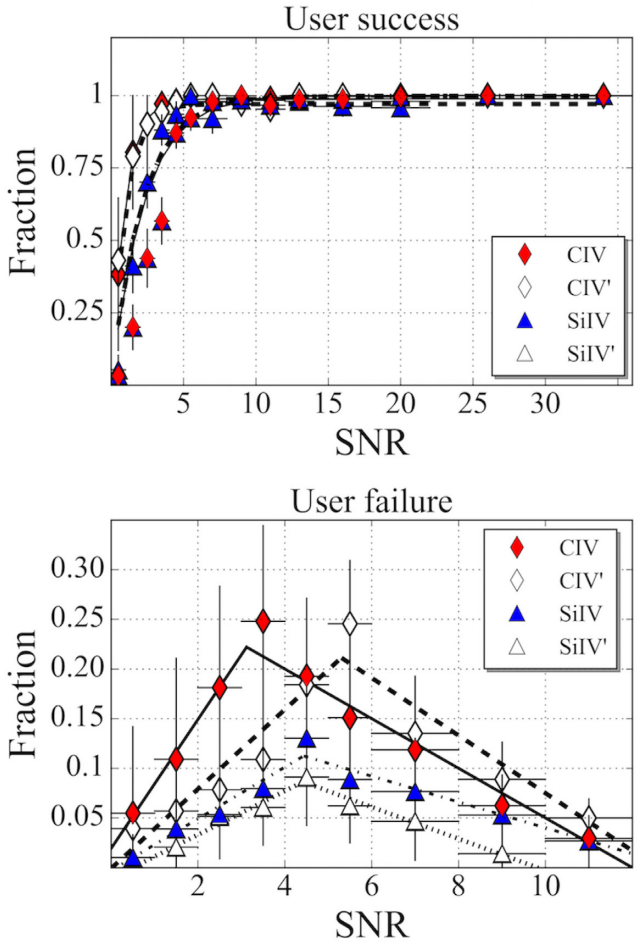

Figure 3. The binned *user success* (top panel; equation 3) and user failure (bottom panel; equation 4) for C IV, C IV′, Si IV, and Si IV′. Plotted with solid, dashed, dot-dash, and dash-dash lines are the respective best fits. The horizontal bounds denote the S/N bin considered and the vertical error bars correspond to the associated 95 per cent Wilson confidence interval.

Table 4. *User success* (equation 3) and *user failure* (equation 4) best-fitting parameters. The best-fittings and binned values can be seen in Fig. 3.

Ion	P_∞	S	$P^{\rm FP}_{\rm max}$	$s_{\rm p}$
C IV	0.97	0.99	0.22	3.12
C IV′	0.98	0.93	0.21	5.30
Si IV	0.99	2.16	0.08	4.42
Si IV′	1.00	2.30	0.11	4.43

in the online appendix. As with the physically spaced doublets, we only consider those artificial systems with a 5σ recovery rate adjusted for *user success* ≥ 0.50. Two C IV′ and one Si IV′ artificial systems survive this selection.

3.4 Adjusting for varying completeness and false positives

Given the fine resolution of the recovery rate adjusted for *user success* (equation 5 and Fig. 4) we must account for this variability across a larger bin of interest in order to derive meaningful statistics. As in C17, we first define a visibility function $R(dz_j)$. It is defined as 1 redward of the Ly α emission peak to within 3000 km s^{-1} of the QSO emission redshift of the *ion* in question

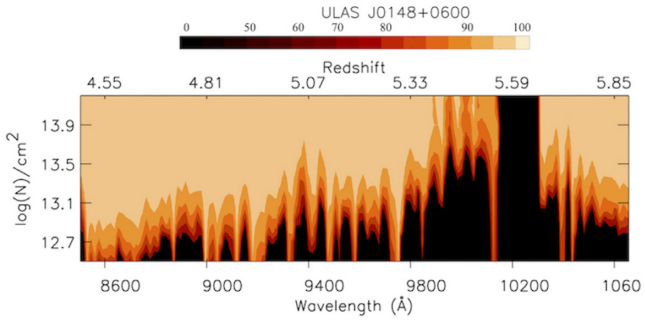

Figure 4. Example C IV 5σ completeness test results for the ULAS J0148+0600 sightline. The x- and y-axes represent the wavelength (Å) and column density (log(N)/cm^2), respectively, of inserted systems. The top x-axis represents the corresponding redshift of an inserted system. Their recovery rate, C(dN_{1548}, dz), is denoted by the colour bar plotted in each panel. All recovery rates below 50 per cent are shaded in black. Recovery rates for all sightlines and for both *real* and *artificial* doublets are presented in sections F and G of the online appendix. The wavelength resolution of the recovery function, C(dN_{1548}, dz), allows us to identify clean portions of the spectra as can be seen in panel *A* at around ∼10 100 Å where the recovery rate is above 50 per cent for even the weakest of inserted systems.

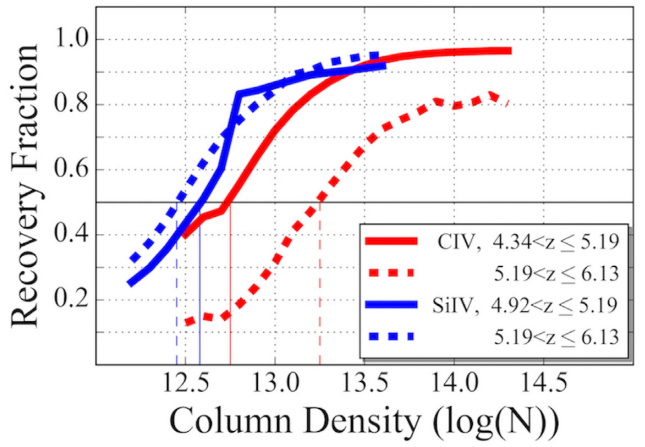

Figure 5. Recovery rates adjusted for *user success* (equation 7) for C IV and Si IV. The vertical lines denote the log($N_{\rm sys}$/cm^2) values down to which we are 50 per cent complete (12.45, 12.58, 12.75, and 13.25, respectively). The recovery of C IV past $z = 5.19$ drops as the redshift pushes the absorbers into the near infra-red.

and 0 everywhere else. We combine equation (5) with this visibility function and re-define the recovery rate adjusted for *user success*

$$C(\log(N), dz_j) = \begin{cases} 0 & \text{if} \quad C(\log(N), dz_j) < 0.50, \\ 1 & \text{if} \quad C(\log(N), dz_j) \geq 0.50 \& R(dz_j) = 1. \end{cases} \tag{6}$$

This formulation identifies all redshift bins (dz_j) in which a single component with column density log($N_{\rm sys}$/cm^2) will be identified in our analysis at least 50 per cent of the time. Next, we split the C IV redshift path in two redshift bins such that they cover a similar recovery adjusted redshift path. That redshift mid-point is at $z = 5.19$.

We then bin and find the average recovery rate adjusted for *user success* as a function of the column density log($N_{\rm sys}$/cm^2) of the inserted doublets C IV and Si IV (see Fig. 5). For the respective redshift bins (below and above redshift 5.19), we find that for C IV,

we are at least 50 per cent complete down to $\log(N_{\rm sys}/{\rm cm}^2)$ values of 12.75 and 13.25. For Si IV we are at least 50 per cent complete for $\log(N_{\rm sys}/{\rm cm}^2)$ values of 12.45 and 12.58 in the same redshift bins.

Following this, we define the average of a function in each redshift bin

$$\bar{f}(dz_j) = \frac{\int\int R(dz_j) \times f(\log(N), dz_j) \frac{d^2N}{dz d\log N} dz d\log N}{\int\int R(dz_j) \frac{d^2N}{dz d\log N} dz d\log N} \quad (7)$$

and compute the average recovery rate adjusted for *user success* ($\bar{C}$), the average recovery rate ($\bar{L}$), the average *user success,* ($\bar{A}$) and average *user failure* ($\bar{A}^{\rm FP}$). Using these values, we can then compute the true number of absorbers (N)

$$N \equiv \frac{\ddot{N}}{\bar{C} - \bar{L} \times \bar{A}^{\rm FP}}. \quad (8)$$

In the same redshift bin, the true number of false positives ($N^{'}$) is

$$N^{'} \equiv \frac{\ddot{N}'}{\bar{C}' - \bar{L}' \times \bar{A}'^{\rm FP}} \quad (9)$$

thus, the false positive contamination rate is

$$F = 1 - \frac{N^{'}}{N}. \quad (10)$$

We combine equations (8) and (10) and define a single scalar for each doublet which accounts for the variable completeness and false positive detections in a redshift bin (A; see Table 2)

$$A = \frac{\bar{F}}{\bar{C} - \bar{L} \times \bar{A}^{\rm FP}}. \quad (11)$$

Finally, the true number of absorbers adjusted for completeness and false positive contamination is

$$N = A \times \ddot{N} \quad (12)$$

with associated Poisson error

$$\sigma N \equiv A \times \sqrt{\ddot{N}}. \quad (13)$$

4 ABSORPTION LINE STATISTICS

When investigating the evolution of absorption systems observed in the spectra of QSOs, it is common to calculate their incidence rate (dN/dz), their comoving mass density ($\Omega_{\rm ion}$), and their CDDF. The incidence rate provides a simple accounting on the number of systems discovered over the total redshift path of a survey and the associated $\Omega_{\rm ion}$ (equation 19) provides a direct measurement of all observed number of atomic ions over the same path (equation 16) normalized to the critical density today. Secondly, $\Omega_{\rm ion}$ can also be measured by directly integrating the first moment of the associated CDDF (equation 17). This method has the added benefit of investigating the impact of integration limits on the $\Omega_{\rm ion}$ values. All incidence rates and associated $\Omega_{\rm ion}$ values can be seen in Table 2. All CDDF best-fitting parameters and integration limits can be seen in Table 5.

Table 5. C IV, Si IV, and Mg II best MLE parameters for CDDF functional form (see equation 21). The redshift bins (Δz), column density range ($\Delta \log(N_{\rm sys}/{\rm cm}^2)$), α and B best-fitting values, and 1σ errors are presented below and are plotted in Figs 10–13. For consistency with D13, we use $\log(N_0) = 13.64$.

Ion	Δz	$\Delta \log(N_{\rm sys}/{\rm cm}^2)$	α	log (B)
C IV	4.33–5.19	[12.75, 14.75]	1.49 ± 0.13	-13.86 ± 0.08
	5.19–6.13	[13.00, 14.00]	1.96 ± 0.36	-14.33 ± 0.18
Mg II	2.00–3.00	[12.50, 15.00]	1.23 ± 0.16	-14.54 ± 0.14
	3.00–4.00	[13.50, 15.00]	1.00 ± 0.38	-14.83 ± 0.33
	4.00–5.45	[12.75, 16.50]	1.09 ± 0.11	-14.98 ± 0.17
C IV	4.33–5.45	[12.50, 14.75]	1.50 ± 0.12	-13.94 ± 0.07
Mg II		[12.75, 15.00]	1.03 ± 0.13	-15.03 ± 0.21
C IV	4.92–6.13	[12.50, 14.25]	1.22 ± 0.14	-14.29 ± 0.11
Si IV		[12.50, 14.00]	1.46 ± 0.31	-14.77 ± 0.25

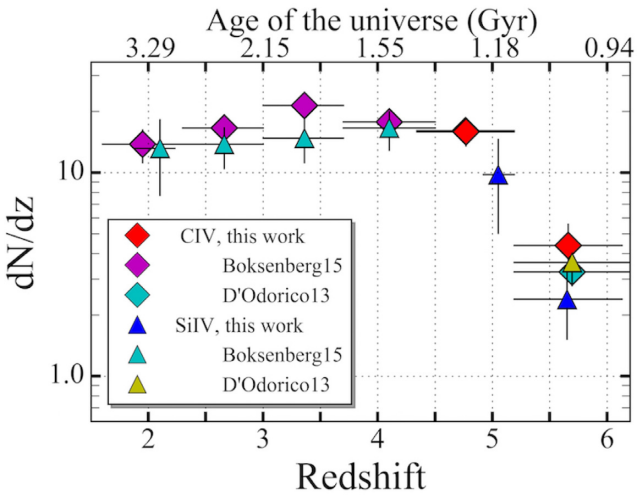

Figure 6. Incidence rates (dN/dz) for C IV and Si IV. The marker style and colours are described in the legend. All values measured with systems described in this work are presented in Table 2. The computation of the D13 values is described in the text. The B15 and S05 values have been adjusted to the *Planck* cosmology used in this work.

4.1 Incidence rates

The true number of absorbers and associated error are computed in equations (12) and (13). This accounts for the contamination by false positives and variable completeness across a redshift bin. The redshift bins are selected so that the C IV path is split in almost half as described in Section 3.4. The incidence rate in a redshift bin (dz) is computed as

$$\left(\frac{{\rm d}N}{dz}\right) = \frac{N \pm \sigma N}{{\rm d}z}, \quad (14)$$

where N is the completeness adjusted and false contamination corrected number of absorbers (equation 12) with associated error σN (equation 13). All incidence rate values computed in this work are presented in Table 2 and can be seen Fig. 6.

For C IV, we compute dN/d$z = 15.4 \pm 2.8$ at a median redshift $\langle z \rangle = 4.77$ and find that it drops by almost a factor of ∼3.5 with dN/d$z = 4.4 \pm 1.2$ at a median redshift $\langle z \rangle = 5.66$. For Si IV, we find a similar evolution with the incidence rate dN/d$z = 9.8 \pm 4.7$ at a median redshift $\langle z \rangle = 5.05$ dropping to dN/d$z = 2.4 \pm 0.9$ at a median redshift $\langle z \rangle = 5.66$.

In order to compare with the survey data of D13 we search their tables A1–A6. We count a total of 79 C IV systems, 62 below redshift 5.19 ($dz = 3.86$), and 17 above redshift 5.19 ($dz = 5.24$). This leads to the C IV incidence rates $dN/dz = 16.1 \pm 2.0$ at a mean redshift $z = 4.76$ and $dN/dz = 3.2 \pm 0.8$ at a mean redshift $z = 5.69$. They are in good agreement with our incidence rate (including system 9 in *ULAS J*1319 + 0959). If system 9 is excluded, as it is the only manually introduced absorber as discussed in Section 2.4.4, then $dN/dz = 3.7 \pm 1.1$. This value is still in good agreement with the D13 values.

We also count 19 Si IV systems, all above redshift 5.19 across a redshift path $dz = 5.24$. This leads to an incidence rate $dN/dz = 3.6 \pm 0.8$ at a mean redshift of $z = 5.69$. Our incidence rates are well within the error bounds. This is not surprising given that 2 out of our 4 sight lines are in common with D13, whose total sample size is 6 QSOs. The incidence rates computed from the D13 tables are plotted in Fig. 6.

Next, we consider if our definition of a system introduces a systematic difference between our incidence statistics and those of D13. We count system 5 in sightline *ULAS J*0148 + 0600, system 10 in sightline *SDSS J*0927 + 2001 and system 3 in sightline *SDSS J*1306 + 0356 as individual systems (see the online appendix). This definition could possibly underestimate the incidence rate in the respective redshift bins. However, this affects only 2 of the 37 C IV systems below redshift 5.19 and only 1 of the 8 C IV systems above redshift 5.19. The possible relative contribution to the incidence rates resulting from the system definition is then 5.4 per cent and 12.5 per cent, respectively. We then find that our system definition does not introduce a systematic given that the respective relative Poisson errors (see Table 2) are several times larger.

Following this, we also compare with the incidence rates from B15. We find that both the incidence rates of C IV and Si IV exhibit a flat evolution until $z \sim 5$. When we consider the incidence rates of B15 only, we compute a mean incidence rate for C IV $<dN/dz> = 17.4 \pm 4.2$. Similarly, for Si IV we compute a mean incidence rate $<dN/dz> = 14.6 \pm 3.8$. Both values are well within the error bounds of the incidence rates computed in this study below redshift 5.19. The B15 values are also plotted in Fig. 6.

Next, we compute the comoving incidence rates (dN/dX) by calculating the absorption path of our survey, noting that a flat behaviour in dN/dX represents no comoving evolution in the cross-section of the population considered. The absorption distance is defined as

$$X(z) = \frac{2}{3\Omega_M}\left[\Omega_M(1+z)^3 + \Omega_\Lambda\right]^{1/2} \quad (15)$$

thus for a redshift bin $[z_1, z_2]$ with $z_2 > z_1$, the absorption path between z_2 and z_1 is

$$dX_{(z_1,z_2)} = X(z2) - X(z1). \quad (16)$$

For C IV we compute $dN/dX = 3.6 \pm 0.6$ at a median redshift $\langle z \rangle = 4.77$ and $dN/dX = 0.9 \pm 0.3$ at a median redshift $\langle z \rangle = 5.66$ while for Si IV we compute $dN/dX = 2.2 \pm 1.1$ at a median redshift $\langle z \rangle = 5.05$ and $dN/dX = 0.5 \pm 0.2$ at a median redshift $\langle z \rangle = 5.66$. We find that the comoving incidence rates of C IV and Si IV are not consistent with a no evolution scenario and both decrease from redshift ~5 to 6.

4.2 Comoving mass densities

The comoving mass density is defined as the first moment of the CDDF normalized to the critical density today

$$\Omega_{\rm ion} = \frac{H_o m_{\rm ion}}{c\rho_{\rm crit}} \int N f(N) {\rm d}N, \quad (17)$$

where $m_{\rm ion}$ is the mass of an ion, $\rho_{\rm crit}$=1.89 × 10^{-29} h^2g cm^{-3} and $f(N)$ is the CDDF. In practice, it is approximated as

$$\Omega_{\rm ion} = \frac{H_o m_{\rm ion}}{c\rho_{\rm crit}} \frac{1}{dX} \sum_s \sum_{\ddot{N}} \sum_k N({\rm ion}), \quad (18)$$

where s represents the number of sightlines with $\ddot{N}$ discovered systems over absorption path dX, each with k components with respective column density N(ion). Given that equation (18) accounts for all k components of all $\ddot{N}$ discovered systems, it is not then susceptible to any bias resulting from the definition of a system. In order to implement the same completeness and false positive corrections described in Section 3.4, we combine equation (18) with equation (11) and calculate $\Omega_{\rm ion}$ as

$$\Omega_{\rm ion} = \frac{A}{dX} \frac{H_o m_{\rm ion}}{c\rho_{\rm crit}} \sum_s \sum_{\ddot{N}} \sum_k N_{\rm sys}({\rm ion}). \quad (19)$$

All A, dX, and $\ddot{N}$ values are presented in Table 2. The associated errors are calculated by first bootstrapping 1000 times across the $\log(N_{\rm sys}/{\rm cm}^2)$ values of each system used. A system can be selected multiple times or not at all. The resulting errors correspond to the 66 per cent confidence interval of the resulting distribution. The B15 and D13 values have been adjusted to the *Planck* cosmology used in this work.

4.2.1 *The comoving mass density of CIV*

We compute the comoving mass density of C IV at the median redshifts $\langle z \rangle = 4.77$ and $\langle z \rangle = 5.66$ and find that, as in previous studies, it drops by approximately a factor of ~4.7 from $1.6^{+0.4}_{-0.1}$ × 10^{-8} to $3.4^{+1.6}_{-1.1}$ × 10^{-9}, respectively.

We plot our values along with those from other studies in Fig. 7. If we do not include system 9 in sightline *ULAS J*1319 + 0959 we compute $\Omega_{\rm C\,IV} = 1.3^{+0.4}_{-0.1} \times 10^{-9}$. The higher redshift Bosman et al. (2017) value is an upper limit on $\Omega_{\rm C\,IV}$ at $\langle z \rangle = 6.6$. The dashed line represents the evolution of $\Omega_{\rm C\,IV}$ from the reference simulation of García et al. (2017, hereafter G17)[10]. In that work, a thousand lines of sight have been generated randomly inside the simulated box. The resulting spectra are first convolved with the instrumental resolution of the VLT-UVES spectrograph and then noise is added to reproduce the typical S/N of observational data. Within each sightline, C IV individual absorption features have been searched for and fitted with VPFIT.

The methodology described in G17 thus mimics the work flow of observational studies but is not impacted by observational constraints such as sky-line emission in the NIR. The synthetic absorption systems with column densities span the column density range $13.8 \leq \log(N/{\rm cm}^2) \leq 15.0$ are summed up to calculate $\Omega_{\rm C\,IV}$. This column density range selection for synthetic absorbers follows the findings by D13. The C IV systems discovered in this study spans $13.00 \leq \log(N/{\rm cm}^2) \leq 14.0$.

[10]Ch 18 512 MDW in their Table 1.

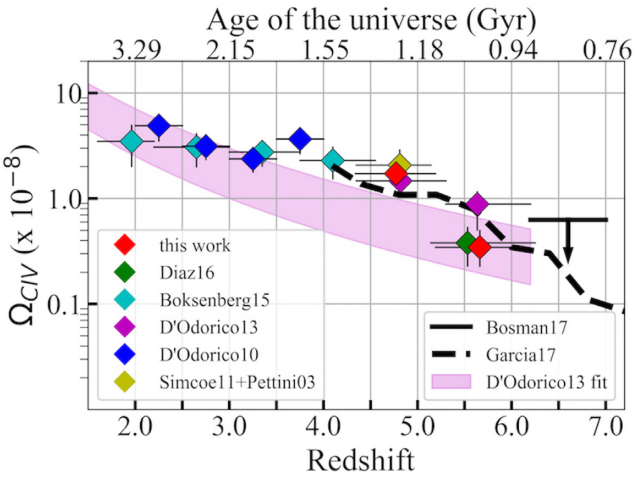

Figure 7. The evolution of the comoving mass densities of C IV as measured in this work along with other observational values from literature and the simulation of G17. The line and marker style and colours are described in the legend.

4.2.2 The comoving mass density of SiIV

We present, for the first time, the comoving mass density of Si IV ($\Omega_{\rm Si\,IV}$) beyond redshift 5. The values of B15 and Songaila (2005, hereafter S05) are adjusted to the *Planck* cosmology used in this work and can be seen, along with our values, in Fig. 8. Given that we only have 2 Si IV systems below redshift 5.19, we simply consider the lower and upper $\log(N_{\rm sys}/{\rm cm}^2)$ bounds of each component and compute the error boundary. We measure $\Omega_{\rm Si\,IV}$=$4.3^{+2.1}_{-2.1}$ $\times\ 10^{-9}$ at a median redshift $\langle z\rangle = 5.05$ and find that it drops to $\Omega_{\rm Si\,IV}$=$1.4^{+0.6}_{-0.4}$ $\times\ 10^{-9}$ by the median redshift $\langle z\rangle = 5.66$.

Interestingly, the G17 simulation, which accurately reproduces the evolution of $\Omega_{\rm C\,IV}$, also reproduces the observed relative evolution of $\Omega_{\rm Si\,IV}$. However, it overproduces Si IV by an order of magnitude when considering the column density range $13.00 < \log(N/{\rm cm}^2) < 15.00$ (dot-dash line Fig. 8). If the comparison is restricted to the column density range of the systems discovered in this study ($12.50 < \log(N/{\rm cm}^2) < 14.00$) then they measure $\Omega_{\rm Si\,IV} = 3.04 \times 10^{-9}$ which is within 3σ of our measured values (see Table 2). We will discuss this in further detail in Section 5.1.

4.3 Column density distribution functions

We compute the respective CDDF for each ion in the following manner

$$f(N) = \frac{\rm n}{\Delta \log(N_{\rm sys})} \times \frac{1}{{\rm d}X}, \tag{20}$$

where $N_{\rm sys}$ is the total column density of a system, n is the number of completeness corrected systems in the column density bin considered ($\Delta\log(N_{\rm sys})$), and dX is the comoving redshift path (equation 16). The completeness functions associated with each redshift bin for C IV and Si IV can be seen in Fig. 5. We then perform a power law fit to the column density distribution

$$f({\rm N}) = B \times \left(\frac{N_{\rm sys}}{N_0}\right)^{-\alpha}, \tag{21}$$

where $N_0 = 10^{13.64}$. We adopt this value for N_0 in order to compare to the work of D13.

We follow the prescription put forth in B17 and take a maximum-likelihood expectation (MLE) approach. We simultaneously fit for α and B and the likelihood function is defined as

$$L(\alpha, B) = P(n|\alpha, B) \times \Pi P(N_{{\rm sys}_i}|\alpha), \tag{22}$$

where $P(n\,|\,\alpha, B)$ is the Poisson probability of observing n systems given a single instance of α and B. We normalize $\Pi P(N_{{\rm sys}_i}\,|\,\alpha)$ so that the expected number of systems is n. The redshift boundaries and transitions considered and best-fitting values with 1σ errors are presented in Table 5. We also investigate if the choice of N_0

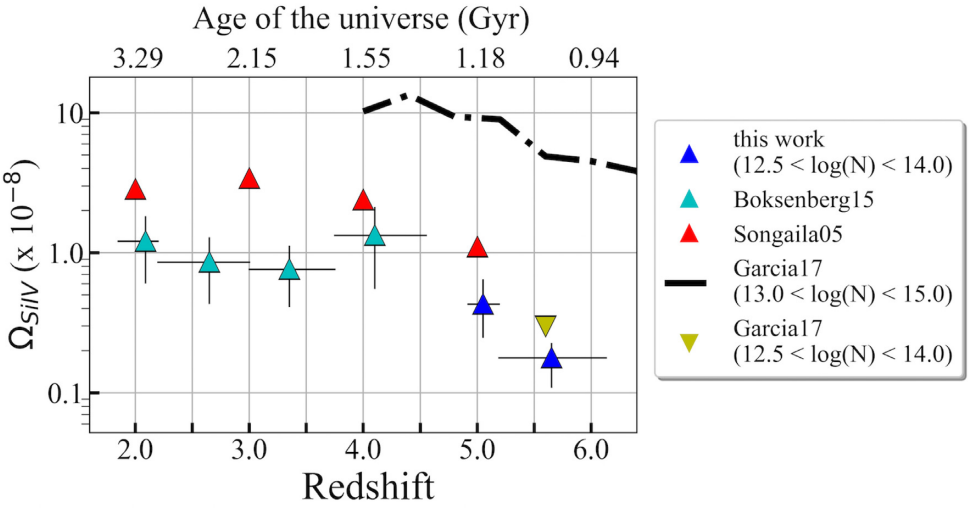

Figure 8. The evolution of the comoving mass densities of Si IV as measured in this work along with other observational values from literature and the simulation of G17. The marker style and colours are described in the legend. The B15 and S05 values have been adjusted to the *Planck* cosmology used in this work.

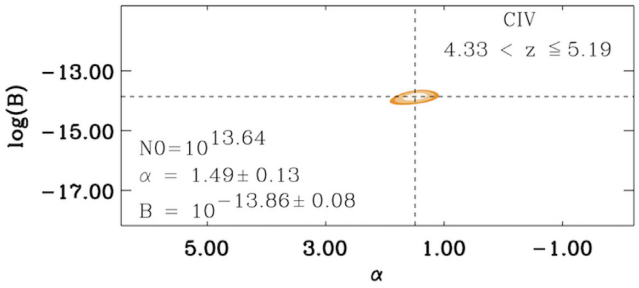

Figure 9. Example CDDF best-fitting 3σ contour plots for all fit parameters (see equation 21) presented in Table 5. All CDDF best fits are presented in the online appendix.

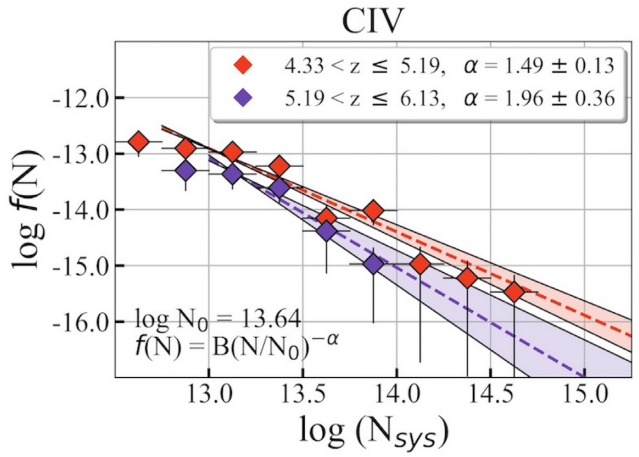

Figure 10. C IV CDDF in two redshift bins. We use Poisson vertical error bars and the horizontal bars denote the column density range of each bin. The marker style and colours are described in the legend. All best-fitting values and 1σ errors are presented in Table 5. The best fits are plotted with a dashed line and the 1σ error bounds are shaded with colours consistent with those of the markers.

impacts our results as B17 used $\log(N_0) = 13.50$ and find that the new values are well within the range of values presented in Table 5. The contour plots of each fit are presented in section H of the online appendix. An example can be seen in Fig. 9. The binned values in Figs 10–15 are presented for a by eye comparison to the best fits obtained through the MLE method discussed above.

First, we fit the C IV CDDF and the best-fittings and binned values can be seen in Fig. 10. We investigate the impact of the lowest column density considered as the C IV CDDF appears to flatten below $\log(N_{sys}/cm^2) = 13.25$. We exclude the lowest column density bin and do not find a significant impact on the final fit parameters. For example, when we use the full range of $\log(N_{sys}/cm^2)$ in the redshift range $4.33 < z \leq 5.19$ we find the best-fitting values $\alpha = 1.49 \pm 0.13$ and $\log(B) = -13.86 \pm 0.08$. If we limit the range to those C IV systems with $\log(N_{sys}/cm^2) \geq 12.75$, we find the best-fitting values $\alpha = 1.69 \pm 0.13$ and $\log(B) = -13.79 \pm 0.08$. We find that the best-fitting α parameter increases to 1.96 ± 0.36 as we move beyond redshift 5.19.

Our values are within 1σ of the D13 values who measures $\alpha = 1.62 \pm 0.2$ ($4.36 < z < 5.3$) and $\alpha = 1.44 \pm 0.3$ ($5.3 < z < 6.20$). A point of difference is that our column density fitting range does not extend beyond $\log(N_{sys}/cm^2) = 14.00$ in our highest redshift bin ($5.19 < z \leq 6.13$) as in the D13 study.

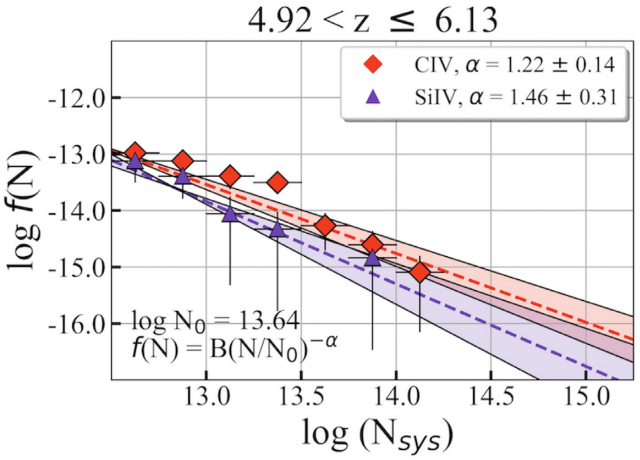

Figure 11. C IV and Si IV CDDF for systems in the same redshift bin. The key to the plotted values, errors, and best-fittings match the description in Fig. 10.

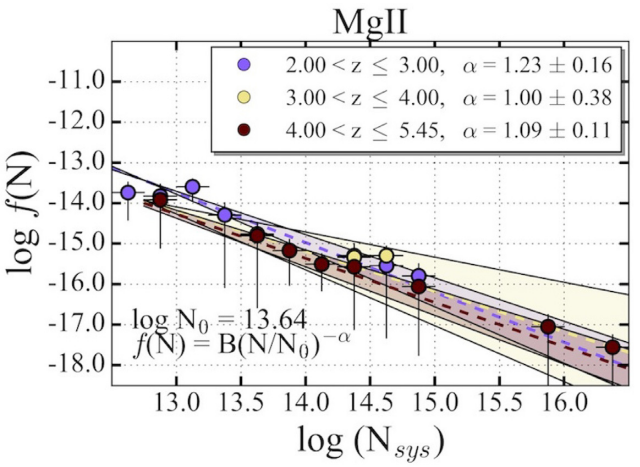

Figure 12. Mg II CDDF in increasing redshift order. The key to the plotted values, errors, and best-fittings match the description in Fig. 10.

Next, we compare the C IV and Si IV CDDFs in the same redshift range across the redshift range for which they can be both observed: $4.92 < z \leq 6.13$. The results can be seen in Fig. 11. For the Si IV CDDF we compute the best-fitting values $\alpha = 1.46 \pm 0.31$ and $\log(B) = -14.77 \pm 0.25$ (see Table 5). When considering the redshift boundary $5.19 < z \leq 6.13$ we find that the C IV α best-fitting parameter does not increase, but rather decreases to $\alpha = 1.22 \pm 0.14$. This change is driven by the lack of systems with $\log(N_{sys}/cm^2) > 14.25$. We see this fluctuation as reflecting the uncertainty associated with our small sample size but we do again highlight that, in all redshift bins, our best-fitting parameterswithin 1σ of the D13 values.

We also present, for the first time, the Mg II CDDFs and best fits in three redshift bins in the full redshift range $2.0 < z \leq 5.45$. The results are based on the 5σ recovery selected systems reported in C17 and can be seen in Table 5 and Fig. 12. We find that the best-fitting parameter α is consistent with $\alpha = 1.23 \pm 0.16$ in the redshift range $2.0 < z < 3.0$ and $\alpha = 1.09 \pm 0.11$ in the redshift range $4.0 < z \leq 5.45$. Finally, we compute the C IV and Mg II CDDFs across the redshift range for which they can be both observed: $4.33 < z \leq 5.45$. The binned values and best fits can be seen in Fig. 13.

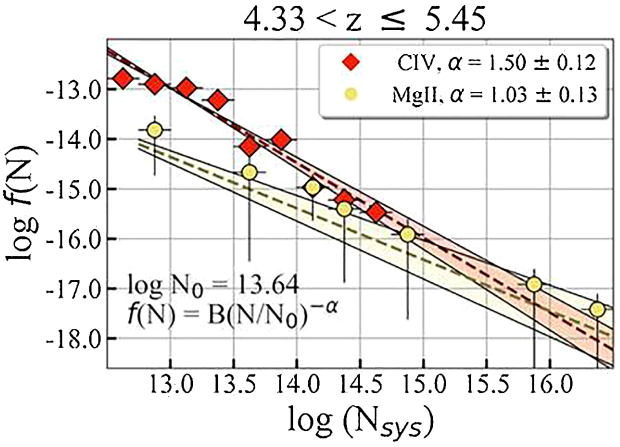

Figure 13. C IV and Mg II CDDF for systems in the same redshift bin. The key to the plotted values, errors, and best-fittings match the description in Fig. 10.

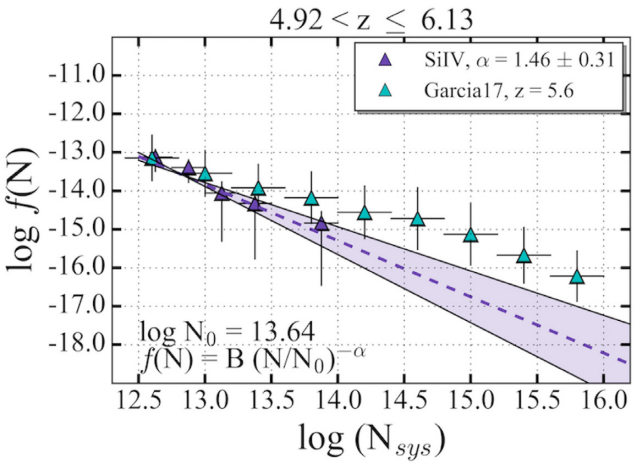

Figure 14. Si IV CDDF for systems in the redshift bin $4.92 < z \leq 6.13$. The key to the plotted values, errors and best-fittings match the description in Fig. 10.

5 DISCUSSION

We measure, for the first time, the incidence rates and comoving mass density of Si IV ($\Omega_{\rm Si\,IV}$) beyond redshift 5.5 and provide additional measurements on the incidence rates and comoving mass density of C IV ($\Omega_{\rm C\,IV}$) beyond redshift 4.33. All values computed in this study are presented in Table 2 and can be seen in Figs 6–8.

The statistics associated with the C IV and Si IV doublets are adjusted for the human impact (see Section 3.2) on the output of an automated detection algorithm (see Section 2.2). We adjust for the likely contamination by false positive detections and varying completeness across redshift bins (see Section 3.4). We use the completeness adjusted values to compute (equation 20) and fit (equation 21) the CDDFs of the Si IV and C IV systems identified in this work as well as the that of the Mg II systems provided in Codoreanu et al. (2017). The best-fitting MLE parameters of the fitting functions are provided in Table 5 and can be seen in Figs 10–13.

Our study is the first to provide a comprehensive survey which compares both *low-* and *high-ionization* systems beyond redshift $z = 5$. Below we compare to the fiducial model of García et al. (2017, G17); we also discuss the physical connection between *low-* and *high-ionization* absorbers.

5.1 Si IV systems

First, we focus on the Si IV systems identified in this work. As we have seen in Section 4.2.2, and as expected, the column density range of the CDDF impacts the computed $\Omega_{\rm Si\,IV}$. The results from the simulation of G17 are in remarkable agreement when restricted to the column density range of Si IV systems discovered in this study ($12.50 \leq \log(N_{\rm sys}/{\rm cm}^2) \leq 14.0$; see Table 5) but differs by approximately an order of magnitude when we compare to the column density range $13.00 \leq \log(N_{\rm sys}/{\rm cm}^2) \leq 15.00$ (dot-dash line in Fig. 8).

In order to investigate this behaviour, we plot our CDDF values and best fits with the binned CDDF values from G17 (see Fig. 14). As can be observed, the two distributions are in good agreement only up to $\log(N_{\rm sys}/{\rm cm}^2) \sim 14.00$. For values of $\log(N_{\rm sys}/{\rm cm}^2) > 14.00$, the Si IV CDDF of G17 disagrees with the extrapolation of the functional fit to the observed distribution. In order to investigate whether the Si IV CDDF of G17 could be representative of the true Si IV population, we ask how many Si IV systems with $\log(N_{\rm sys}/{\rm cm}^2) > 14.00$ we should have observed over the absorption path of our survey ($\Delta X_{\rm Si\,IV} = 16.40$; see Table 2).

We consider the CDDF of G17 in the column density range $14.4 \leq \log(N_{\rm sys}/{\rm cm}^2) \leq 14.8$. We find that we should have detected ∼12 Si IV absorbers within the column density range considered. We observe none. Next, we consider the case that the CDDF fit of this work extends past $\log(N_{\rm sys}) \sim 14.00$ and use the best-fitting values in Table 5 for the redshift range $4.92 \leq z \leq 6.13$. When considering the same column density range we calculate an expectation of ∼0.4 absorbers. This suggests that future surveys which will increase $\Delta X_{\rm Si\,IV}$ to beyond ∼40 should observe a Si IV system with $14.4 \leq \log(N_{\rm sys}/{\rm cm}^2) \leq 14.8$. Future surveys with enough path length to at least detect one such system will be able to better address this issue.

While we do not detect any systems with column densities between $14.00 < \log(N_{\rm sys}/{\rm cm}^2) < 15.00$ we can investigate their impact on the associated Ω value. We integrate the first moment of the Si IV CDDF and compute the resulting $\Omega_{\rm Si\,IV}$ value (see equation 17) in the redshift range $4.92 < z \leq 6.13$ and column density range $12.50 < \log(N_{\rm sys}/{\rm cm}^2) < 15.00$. We compute an expectation of $\Omega_{\rm Si\,IV} = 5.6^{+11.7}_{-3.5} \times 10^{-9}$. Next, we combine the $\Omega_{\rm Si\,IV}$ values measured in this study from Table 2 and find that across the same redshift bin we measure $\Omega_{\rm Si\,IV} = 5.7^{+2.7}_{-2.5} \times 10^{-9}$. This suggests that the contribution to $\Omega_{\rm Si\,IV}$ from future detections of Si IV with $14.00 < \log(N_{\rm sys}/{\rm cm}^2) < 15.00$ will be minimized by the large absorption path necessary to discover them.

Given then that our measured $\Omega_{\rm Si\,IV}$ value is not biased by the lack of Si IV systems with $\log(N_{\rm sys}/{\rm cm}^2) > 14.00$, we next look at the relative evolution of Si IV from below to above $z \sim 5$. Our motivation for this is to compare to the relative evolution of $\Omega_{\rm C\,IV}$ which drops by a factor of 2–4 across the same redshift range (D13 and references therein). We adjust the highest redshift values from B15 to the cosmology used in this paper and find $\Omega_{\rm Si\,IV} = 1.4 \pm 0.8 \times 10^{-8}$ at $\langle z \rangle = 4.10$. When we compare to the $\Omega_{\rm Si\,IV}$ measured in this study (see Table 2), we find that $\Omega_{\rm Si\,IV}$ drops by a factor of 3 ± 2 from $\langle z \rangle = 4.10$ to $\langle z \rangle = 5.05$. By $\langle z \rangle = 5.66$ that factor increases to 10 ± 7.

For comparison we calculate the fractional evolution of $\Omega_{\rm C\,IV}$ using systems identified in this work (see Table 2) and find that $\Omega_{C\,IV}$ decreases by a factor of 5 ± 2 from $\langle z \rangle = 4.77$ to $\langle z \rangle = 5.66$. While this seems to suggest that $\Omega_{Si\,IV}$ and $\Omega_{C\,IV}$ have similar evolutions from below to beyond redshift 5 we again highlight that

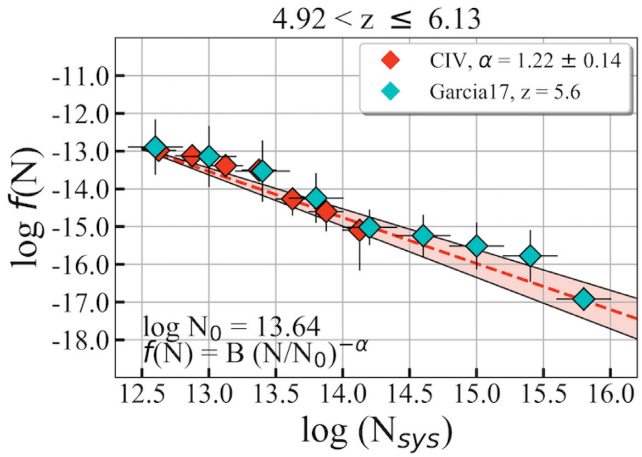

Figure 15. C IV CDDF for systems in the redshift bin $4.92 < z \leq 6.13$. The key to the plotted values, errors, and best-fittings match the description in Fig. 10.

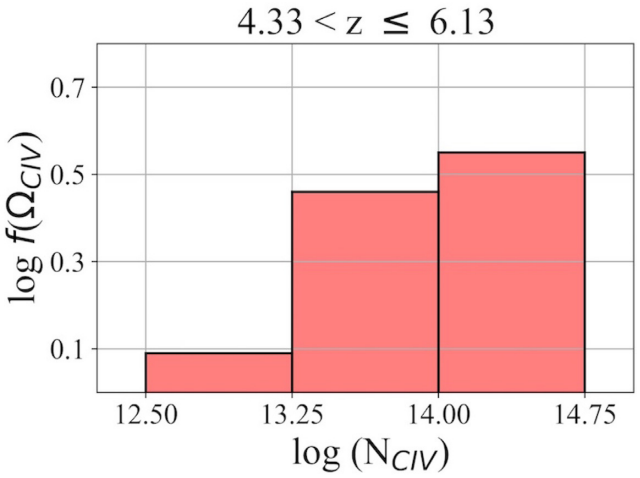

Figure 16. The fractional contribution to $\Omega_{\rm C\,IV}$ as measured in this study in $\Delta \log(N_{\rm C\,IV})$ bins as defined in equation (23).

our work is the only study, so far, to provide information on $\Omega_{Si\,IV}$ beyond redshift 5.5. Future studies will be able to provide further insight on this evolution.

Interestingly, five of the seven Si IV systems also have associated C IV. All of these Si IV systems have $\log(N_{\rm sys}/{\rm cm}^2) \geq 12.75$. Two of these systems, 8 and 9 in *ULAS J*1319 + 0959, also have associated *low-ionization* systems, Mg II+Al II(λ1670) and C II(λ1334)+Al II(λ1670), respectively. As Finlator et al. (2016) have pointed out, Si IV (∼3.3 Ry) is an intermediary transition between C II (1.8 Ry) and C IV (∼4.7 Ry). Thus, constraining both the relative evolution of Si IV, C IV, and C II as well as the number density and nature/environment of Si IV and C IV systems with $\log(N_{\rm sys}/{\rm cm}^2) > 14$ is necessary in order to discriminate between different UVB or hydrogen self-shielding prescriptions. Given that we do not identify any Si IV systems with $\log(N_{\rm sys}/{\rm cm}^2) > 14$ and that all Si IV systems with $\log(N_{\rm sys}/{\rm cm}^2) > 12.75$ identified in this study have associated C IV we next investigate the population of C IV absorbers identified in this work.

5.2 CIV systems

As we have seen in Section 4.3, and as expected, the CDDF slope is sensitive to both the sample size and the column density range of the fit. For example, the best-fitting parameter α increases from 1.22 ± 0.14 to 1.96 ± 0.36 when the column density range changes from $\Delta\log(N_{\rm sys}/{\rm cm}^2) = [12.50, 14.25]$ to $\Delta\log(N_{\rm sys}/{\rm cm}^2) = [13.00, 14.00]$ and sample size decreases from 13 to 6 systems (see Figs 10 and 11, respectively).

As in the previous section, we compare the C IV CDDF and best fits computed in this work with the C IV G17 CDDF. The results can be seen in Fig. 15. We find that both CDDFs are in excellent agreement in the column density range of the systems discovered in this work $\Delta\log(N_{\rm sys}/{\rm cm}^2) = [12.50, 14.25]$. Unlike the Si IV CDDFs discussed in the previous section, the C IV CDDF of G17 is in excellent agreement with an extrapolation of the functional fit to the C IV CDDF computed in this work, $\log(N_{\rm sys}/{\rm cm}^2) > 14.25$.

As we have discussed in the previous section, the comoving mass density is sensitive to the column density range considered. We quantify this influence by computing the fractional contribution, $f(\Omega_{\rm C\,IV})$, from each column density bin, $\Delta\ \log(N_{\rm C\,IV})$, considered in Section 4.3 to the total computed $\Omega_{\rm C\,IV}$:

$$f(\Omega_{\rm C\,IV}) = \frac{\Omega_{\Delta\log(N_{\rm C\,IV})}}{\Omega_{\rm C\,IV}}. \quad (23)$$

We find that C IV systems with $\log(N_{\rm sys}/{\rm cm}^2) \geq 14.00$ contribute more than 50 per cent to the comoving mass density of C IV computed in this work, $\Omega_{\rm C\,IV}$. The resulting histogram can be seen in Fig. 16.

In order to further investigate C IV systems with $\log(N_{\rm sys}/{\rm cm}^2) \geq 14.00$, we subdivide the C IV absorber population used in this study in four categories based on whether or not associated absorbers are also identified at the redshift of the C IV doublet. We find

(i) 25 C IV systems *with no associated absorbers;*
(ii) Six C IV systems *with associated low-ionization absorbers*: system 3 in *ULAS J*0148 + 0600, system 5 in *SDSS J*0927 + 2001, systems 2, 8, and 9 in *SDSS J*1306 + 0356, and system 3 in *ULAS J*1319 + 0959;
(iii) Two C IV systems *with associated low- and high-ionization absorbers*: systems 8 and 9 in *ULAS J*1319 + 0959;
(iv) Three C IV systems *with associated high-ionization absorbers*: system 7 in *ULAS J*0148 + 0600, system 8 in *SDSS J*0927 + 2001, and system 6 in *ULAS J*1319 + 0959.

Following this, we compute the velocity width of each absorber (Δv_{90}; Prochaska et al. 2008) and plot the values versus the column density of each system in Fig. 17. We find that four out of the six C IV systems with $\log(N_{\rm sys}/{\rm cm}^2) \geq 14.00$ have associated *low-ionization* absorbers. Furthermore, we find that all C IV systems with $\Delta v_{90} \geq 200\,{\rm km\,s^{-1}}$ have associated *low-ionization* absorbers (five of the eight absorbers). In order to highlight these boundaries, we have plotted dashed lines in Fig. 17.

These findings suggest that C IV absorbers with associated *low-ionization* absorbers contribute significantly to the number density and the comoving mass density of C IV. Furthermore, these same C IV systems are dominated by a sub-population of absorbers with broad velocity profiles ($\Delta v_{90} \geq 200\,{\rm km\,s^{-1}}$). Next, we focus our discussion on the two absorbers with the broadest velocity profiles, systems 8 and 9 in *SDSS J*1306 + 0356.

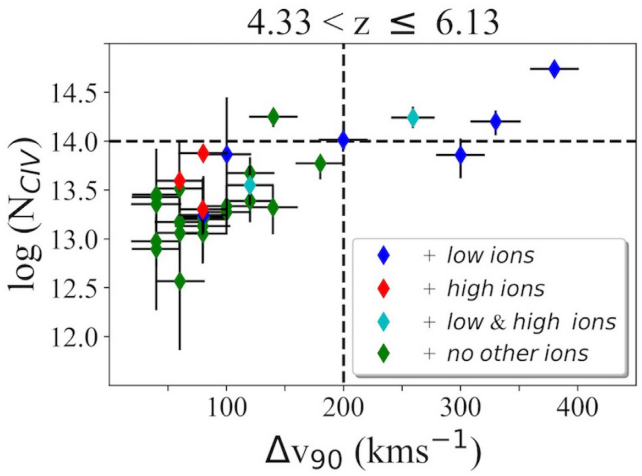

Figure 17. The velocity width (Δv_{90}) versus the column density, $\log(N_{\rm C\,IV})$ of the C IV systems used in this work. The marker style and colours are described in the legend. The labels are described in detail in Section 5.2.

5.3 The physical connection between low- and high-ionization absorbers

As we have previously discussed in Section 2.4.3, we have plotted selected transitions[11] of systems 8 and 9 together in Fig. 18 in order to highlight the proximity and similar velocity structure of the associated absorbers.

Our first question is to assess if the two systems could be associated with a single galaxy. In order to investigate this possibility, we translate the velocity separation between the reddest C IV component of system 8 and bluest Mg II component of system 9 (component *a* in table A3 in C17) into a physical separation. This separation is highlighted by the black vertical dashed lines at +600 and +900 km s^{-1} in Fig. 18 which correspond to redshifts 4.87051 and 4.87638, respectively. The physical distance between the two redshifts is ∼550 kpc.[12] Given that the systems themselves span more than 500 km s^{-1} and are separated by ∼550 physical kpc we find that these two absorption systems are most likely tracing two separate structures rather a fortuitous double intersection of our sightline through a single system.

Understanding the environment of such C IV and Mg II systems is a crucial step as they have a significant impact on the associated CDDFs and comoving mass densities. Previous studies which have investigated similar Mg II absorbers[13] at z < 1 have found that such ultra-strong absorbers reside in group environments. The velocity width of the absorbers can be driven by either star formation (SFR > 5 M$_\odot$ yr^{-1}) driven outflows (Nestor et al. 2011) or intra-group interactions (Gauthier 2013). Furthermore, such strong C IV systems ($\log(N_{\rm sys}/{\rm cm}^2) > 14.0$) have also been connected to dense environments populated with young and blue galaxies in the redshift range $1.8 \leq z \leq 3.3$ (Adelberger et al. 2005). Are then these systems tracing similar physical environments past redshift 5?

Recently, Cai et al. (2017) also investigated the environment of these same C IV absorbers using *Hubble Space Telescope (HST)* narrow band imaging to identify Ly α emitters (LAE). They find a single LAE candidate at an impact parameter of 205 kpc with an associated Ly α luminosity derived star formation rate, SFR$_{{\rm Ly}_\alpha}$ = 2.5 M$_\odot$ yr^{-1}. This would suggest that there are no star forming galaxies with SFR > 5 M$_\odot$yr^{-1} which can be associated with the absorber.

Given that the study of Cai et al. (2017) does not identify multiple star-forming galaxies we favour the hypothesis that the velocity width of the absorbers is driven by tidal interactions between previous outflow material and group members with luminosities below the detection limit of the Cai et al. (2017) study. We find that these Mg II systems likely trace a disturbed environment, a possibility recently raised by Zou et al. (2017) following their study of strong Mg II systems in the redshift range 1.73 < z < 2.43. However, since we currently do not have any information on the associated galaxies, it is difficult to create a complete picture.

Despite this lack of information, the physical association of C IV systems with $\log(N_{\rm sys}/{\rm cm}^2) \geq 14.00$ with *low-ionization* systems and their high velocity width ($\Delta v_{90} \geq 200$ km s^{-1}) suggests that these systems are tracing a multiphase medium where hot and cold gas is mixing at the interface between the CGM and IGM. Thus, in order to accurately simulate the full C IV population of absorbers this physical interaction must be accounted for.

5.4 The comoving mass densities of low-ionization systems beyond redshift ∼2

We have so far provided further measurements of $\Omega_{\rm C\,IV}$ (see Section 4.2.1 and Fig. 7) and presented the first measurement of $\Omega_{\rm Si\,IV}$ (see Section 4.2.2 and Fig. 8) beyond redshift 5. However, as we have discussed in Section 2.2, we also search for other associated transitions at the redshift of the identified doublets. We do not identify any O I systems over the absorption path of our survey (dX = 8.93).

When considering the C IV and Si IV doublets identified in our work, we find 5 Si II, 8 Al II, 6 Fe II, 1 C II, and 2 Mg I associated transitions with $z > 4.33$. These transitions are associated with

(i) systems 3 and 9 in sightline *ULAS J0148+0600*
(ii) system 5 in sightline *SDSS J0927+2001*
(iii) systems 2, 8, and 9 in sightline *SDSS J1306+0356*
(iv) systems 8 and 9 in sightline *ULAS J1319+0959*.

We find a further 2 Al II, 6 Fe II, 5 Mg I, and 1 Ca II associated with Mg II doublets below redshift 4.33. We present these absorbers in the online appendix.

All of these transitions are associated with doublet identified absorbers which have a *user success* and *failure* adjusted recovery rates greater than 50 per cent (see Section 3). As such, we consider these identifications to be robust. We do not adjust their statistics for completeness and compute their associated comoving mass densities using equation (18). The errors are calculated using Poisson statistics. We present the comoving mass densities of Fe II, Si II, C II, Mg I, Al II, and Ca II in Table 6 and Fig. 19. We compare our results with the recent work of Lan & Fukugita (2017, hereafter LF17) which provides the comoving mass densities of these ions along with others not identified in this work up to redshift ∼2.5 as traced by Mg II absorbers.

We find that our $\Omega_{\rm Fe\,II}$ and $\Omega_{\rm Mg\,I}$ values are in excellent agreement with those presented in LF17 at z ∼ 2.5 and exhibit a flat evolution (within 2σ) from redshift 2 to 5.45. This is unsurprising as the Fe II and Mg I transitions are mostly[14] associated with strong Mg II absorbers whose $\Omega_{\rm Mg\,II}$ exhibits a similar behaviour as discussed in

[11] C IV (λ1548), Mg II(λ2796), Si II(λ1526) and Fe II(λ2600).
[12] ∼3.23 comoving Mpc.
[13] With $W_{2796} > 3$ Å.
[14] Except for system 2 in *SDSS J1306+0356* which has $W_{2796} = 0.734 \pm 0.062$ Å.

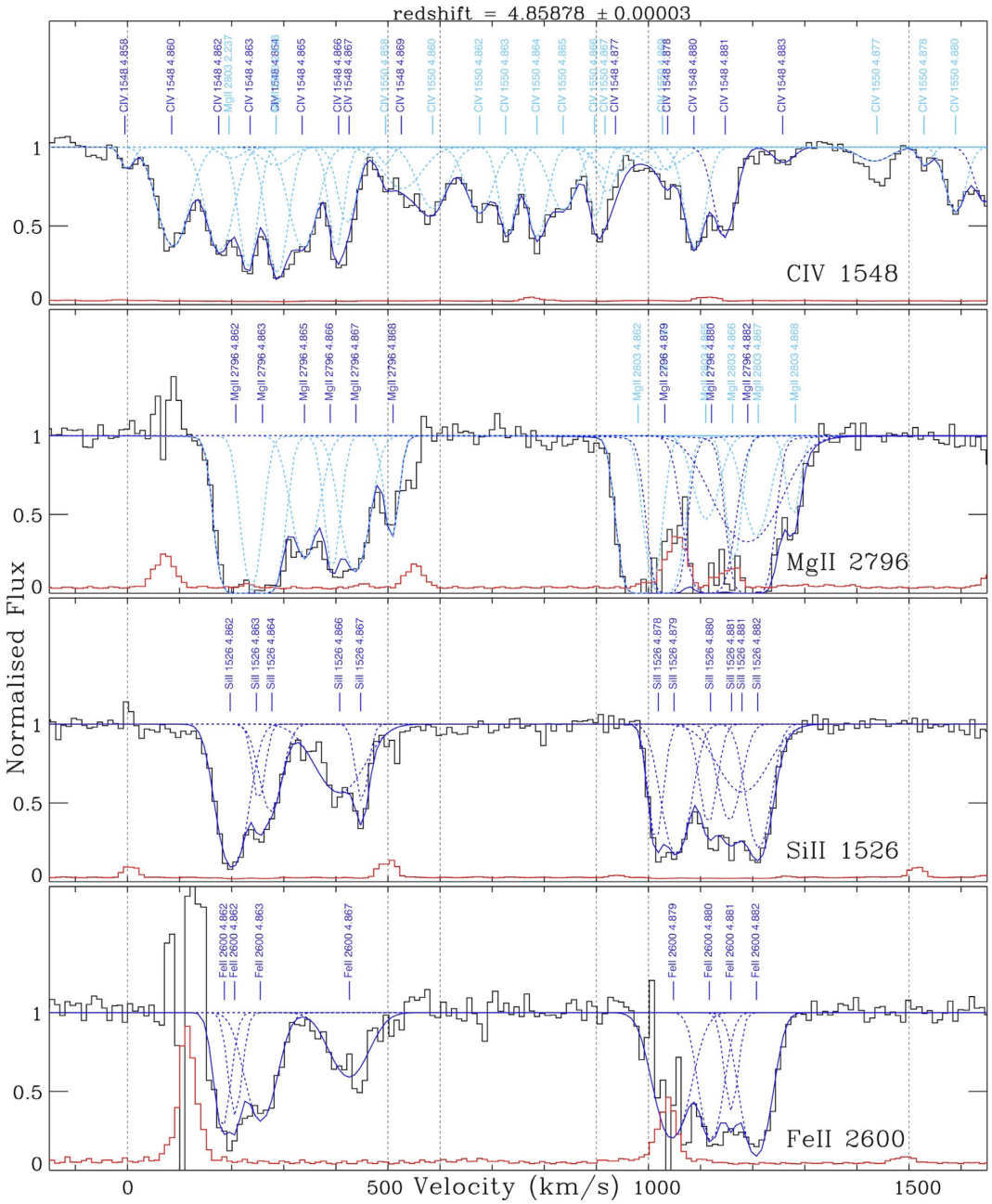

Figure 18. Selected transitions from systems 8 and 9 identified in the *SDSS J1306+0356* sightline. Each transition is identified in the bottom middle of each panel. In each panel, the vertical axis is the continuum normalized flux. The horizontal axis is the velocity separation (km s^{-1}) from the lowest redshift component of a system. The normalized spectrum is plotted in black and the associated error is in red. The solid blue line represents the full fit to the spectra and includes other ions besides the transition identified in the bottom right of each panel (i.e. the C IVλ1550 transition). Individual components are plotted with dashed lines and are identified by a vertical label. The identified transition components are in solid blue and other transitions are in light blue. The black vertical dashed lines highlight the 0, +500, +600, +900, +1000, and the +1500 km s^{-1} velocity locations for reasons discussed in Section 5.3.

C17. We find a similar flat evolution when comparing the value of $\Omega_{\rm Si\,II}$ computed in this work at $\langle z\rangle = 4.61$ ($7.5 \pm 3.8 \times 10^{-8}$) with those of LF17 at z ∼ 2.4 (∼3×10^{-8}). Again, this is not surprising since these Si II and Fe II transitions are associated with the same systems.

Interestingly, we find that $\Omega_{\rm Si\,II}$ drops by ∼3 orders of magnitude from $\langle z\rangle = 4.61$ ($7.5 \pm 3.8 \times 10^{-8}$) to $\langle z\rangle = 5.77$ ($1.8 \pm 1.8 \times 10^{-11}$). We find only one Si II system beyond redshift 5 ($z = 5.77495 \pm 0.00038$; see Fig. 2) and it is anchored by a Si IV doublet. However, just as the Fe II and Mg I systems discussed above, all other Si II identified in this work are mostly[14] associated with *strong* Mg II systems. We see the evolution of $\Omega_{\rm Si\,II}$ from $\langle z\rangle = 4.61$ to $\langle z\rangle = 5.77$ as simply reflecting this association, or lack there of, and further observational studies will be able to confirm this.

Similar to the evolution of Si II from redshift 2 to 5.47, we find that $\Omega_{\rm C\,II}$ also drops by several orders of magnitude from ∼0.5×10^{-7} at $z \sim 2.4$ (LF17) to $6.3 \pm 6.3 \times 10^{-9}$ at $\langle z\rangle = 5.57$ as measured in this work. However, the single C II transition identified in this

Table 6. Median redshifts ($\langle z \rangle$), redshift paths (Δz), absorption distances (dX), discovered systems ($\bar{N}$) and the comoving mass densities (Ω) for C II, Si II, Al II, and Fe II systems used in this work.

Ion	$\langle z \rangle$	Δz	dX	$\bar{N}$	Ω
Si II	4.61	4.41–5.00	7.70	4	$7.5 \pm 3.8 \times 10^{-8}$
	5.77	5.00–6.13	17.59	1	$1.8 \pm 1.8 \times 10^{-11}$
Al II	4.60	4.00–5.00	16.78	8	$2.2 \pm 0.8 \times 10^{-9}$
	5.47	5.00–6.13	17.59	2	$2.4 \pm 1.7 \times 10^{-11}$
Fe II	2.53	2.00–3.00	13.12	4	$2.9 \pm 1.5 \times 10^{-8}$
	3.41	3.00–4.00	15.09	1	$4.5 \pm 4.5 \times 10^{-9}$
	4.61	4.00–5.45	24.84	7	$2.6 \pm 1.0 \times 10^{-8}$
C II	5.57	5.18–6.13	11.32	1	$6.3 \pm 6.3 \times 10^{-10}$
Mg I	2.53	2.00–3.00	13.12	3	$5.7 \pm 3.3 \times 10^{-11}$
	3.41	3.00–4.00	15.09	2	$6.7 \pm 4.7 \times 10^{-11}$
	4.61	4.00–5.45	24.84	2	$5.7 \pm 4.0 \times 10^{-11}$
Ca II	3.41	3.00–4.00	15.09	1	$1.7 \pm 1.7 \times 10^{-11}$

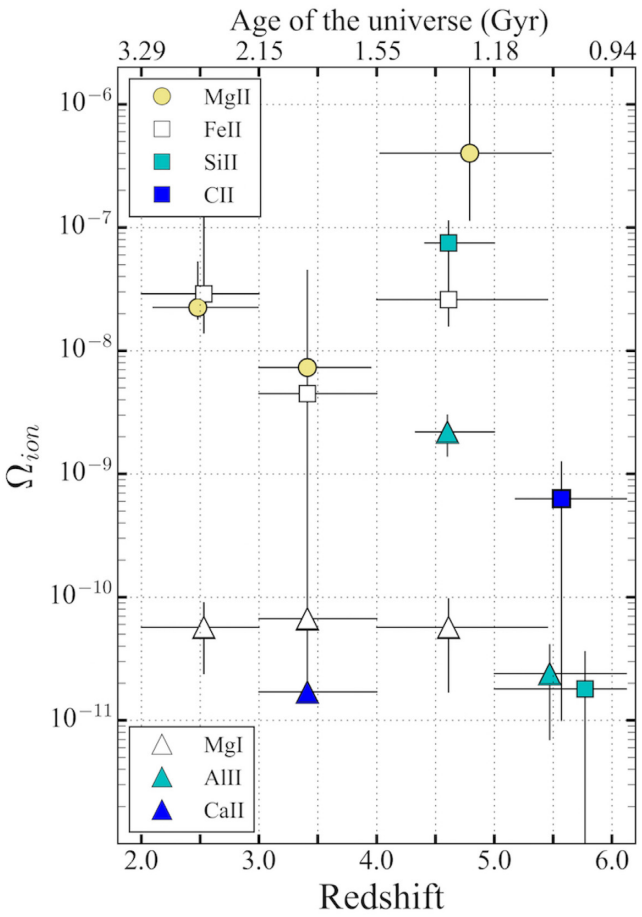

Figure 19. The evolution of the comoving mass densities of Mg I, Ca II, Si II, Al II, Fe II, and C II as measured in this study. The redshift boundaries, median redshifts and computed Ω_{ion} values along with errors can be seen in Table 6. The Mg II values are taken from C17.

work is associated with a single *weak* Mg II absorber while LF17 integrate across the full equivalent width range. When we consider the evolution of Al II we find that it drops by ∼2 orders of magnitude from redshift 4.60 to 5.47. Just as with the Si II and C II ions, the Al II absorbers beyond redshift 5 are associated only with *weak* Mg II absorbers while the Al II absorbers below redshift 4 are mostly associated with *strong* Mg II absorbers. These absorbers dominate the computed $\Omega_{\rm Al\,II}$ at $\langle z \rangle = 4.60$.

We find that $\Omega_{\rm Mg\,I}$ and $\Omega_{\rm Fe\,II}$ have a flat evolution from redshift 2 to 5.45 as measured in this work. When we compare to the findings of LF17, we find a similar evolution for $\Omega_{\rm Si\,II}$ and $\Omega_{\rm Al\,II}$ from redshift 2 to 5. However, from redshift 5 to redshift 6 $\Omega_{\rm Si\,II}$, $\Omega_{\rm C\,II}$, and $\Omega_{\rm Al\,II}$ drop by several orders of magnitude. This evolution results from the association of these absorbers with only *weak* Mg II absorbers while, from redshift 2 to 5, the Si II and Al II identified in this study are mostly associated with *strong* Mg II absorbers. For this reason, we caution the reader in drawing significant conclusions from their evolution as the Si II, Ca II, and Al II populations identified in this work past redshift 5 are clearly limited by small number statistics. We will further investigate the full population and statistics of Mg II absorbers from redshift 2 to 7 in an upcoming paper.

6 CONCLUSION

We investigate four medium resolution and signal-to-noise spectra of $z \sim 6$ QSOs for the presence of C IV, Si IV doublets and associated transitions. These same spectra were investigated for the presence of Mg II doublets in Codoreanu et al. (2017).

We adjust the statistics of the C IV and Si IV systems for the impact of varying signal-to-noise and completeness across the redshift bins considered, the human impact on the identification methodology and false positive contamination. The details are described in Section 3. The incidence rates, absorption paths, and comoving mass density values are presented in Table 2 and can be seen in Figs 6–8.

We also compute the CDDFs (see equation 20) of Si IV, C IV, and Mg II and use a maximum-likelihood estimation (MLE) approach to fit the distributions (see equation 21). The redshift boundaries and column density ranges considered are presented in Table 5 along with the best-fitting parameters and associated errors. The CDDF distributions and best fits are discussed in Section 4.3 and can be seen in Figs 10–13. Our main findings are

(i) We visually identify 41 C IV and 7 Si IV systems with 36 and 7 passing our 5σ selection criteria, respectively. The highest redshift C IV and Si IV absorbers identified in our survey which meet our 5σ selection criteria are, respectively, system 15 in sightline *SDSS J*1306 + 0356 with $z = 5.80738 \pm 0.00017$ and 9 in sightline *ULAS J*0148 + 0600 with $z = 5.77495 \pm 0.00038$. The absorption systems can be seen in the online appendix. An example can be seen in Fig. 2.

(ii) We compute the incidence rates of C IV and Si IV and find that both decrease from redshift ∼5 to 6. For C IV we compute dN/dX = 3.6 ± 0.6 at a median redshift $\langle z \rangle = 4.77$ and dN/dX = 0.9 ± 0.3 at a median redshift $\langle z \rangle = 5.66$. For Si IV we compute dN/dX = 2.2 ± 1.1 at a median redshift $\langle z \rangle = 5.05$ and dN/dX = 0.5 ± 0.2 at a median redshift $\langle z \rangle = 5.66$. The values computed in this work can be seen in Table 2. We combine our non comoving incidence rates with those of D'Odorico et al. (2013) and Boksenberg & Sargent (2015). The results can be seen in Fig. 6 and the details are described in Section 4.1.

(iii) We compute, for the first time, the comoving mass density of Si IV ($\Omega_{\rm Si\,IV}$) beyond redshift 5.5. We measure $\Omega_{\rm Si\,IV} = 4.3^{+2.1}_{-2.1} \times 10^{-9}$ at $\langle z \rangle = 5.05$ and $\Omega_{\rm Si\,IV} = 1.4^{+0.6}_{-0.4} \times 10^{-9}$ at $\langle z \rangle = 5.66$. We combine our findings with the values computed in the observational study of Boksenberg & Sargent (2015) and the simulations of García et al. (2017). We plot the values in Fig. 8. We find that the our

$\Omega_{\rm Si\,IV}$ values agree very well with the expectations from García et al. (2017) when considering the column density range of systems identified in this work ($12.50 < \log(N_{\rm Si\ IV}) < 14.0$). However, when the column density range considered is increased to also include systems with $N_{\rm Si\ IV} < 15.0$, the expected $\Omega_{Si\,IV}$ increases by an order of magnitude. We discuss this in further detail below when comparing the Si IV CDDFs of this work versus those of García et al. (2017). The associated absorption paths, incidence rates, and number of absorbers can be seen in Table 2.

(iv) We also measure the comoving mass density of C IV ($\Omega_{\rm C\,IV}$) beyond 4.34 and find a similar evolution as previous studies (Ryan-Weber et al. 2006; Simcoe 2006; Becker et al. 2009; Ryan-Weber et al. 2009;Simcoe et al. 2011; D'Odorico et al. 2013). We combine our results with those from literature and present them in Fig. 7. We measure $\Omega_{\rm C\,IV} = 1.6^{+0.4}_{-0.1} \times 10^{-8}$ at $\langle z \rangle = 4.77$ and $\Omega_{\rm C\,IV} = 3.4^{+1.6}_{-1.1} \times 10^{-9}$ at $\langle z \rangle = 5.66$. The associated absorption paths, incidence rates, and number of absorbers can be seen in Table 2.

(v) We compute the CDDFs of the Si IV and C IV systems used in this work as well as the Mg II systems presented in Codoreanu et al. (2017). We then perform a MLE functional fit (see equation 21) to the distributions and all best-fitting parameters can be seen in Table 5. We find that our C IV best-fitting parameters are within 1σ of those presented in D'Odorico et al. (2013)

(vi) We compare our Si IV and C IV CDDFs with those presented in and based on the simulations of García et al. (2017) as can be seen in Figs 14 and 15. We find that the C IV CDDFs are in excellent agreement even beyond the range of C IV systems identified in our study ($\log(N_{\rm sys}/{\rm cm}^2) > 14.25$). However, we find that our measured Si IV CDDF only agrees with that of García et al. (2017) in the column density range of the systems discovered in this study ($12.50 < \log(N_{\rm sys}/{\rm cm}^2) < 14.00$). We discuss this in detail in Section 5.1.

(vii) We find that 5 of the 7 Si IV systems have associated C IV transitions and 10 of the 36 C IV systems have associated *low-\high*-ionization systems. We compute the velocity width of the C IV absorbers (Δv_{90}) and plot them versus their $\log(N_{\rm sys}/{\rm cm}^2)$ in Fig. 17. We find that all C IV systems with $\Delta v_{90} > 200\,{\rm km\,s^{-1}}$ have associated *low-ionization* systems.

(viii) We investigate the 2 absorbers with the widest velocity widths, systems 8 and 9 in *SDSS J1306 + 0356*. In order to highlight their complex velocity structures and proximity, we plot them on the same velocity scale zeroed on the first component of system 8 in Fig. 18. These systems are also ultra strong Mg II systems ($W_{2796} > 3$ Å). This class of Mg II absorbers has been associated with both star formation (Nestor et al. 2011) and tidal interactions (Gauthier 2013) in group environments below redshift 1. Recently, Cai et al. (2017) image the *SDSS J1306 + 0356* field using *HST* and find a single LAE with SFR $= 2.5\ {\rm M}_\odot\ {\rm yr}^{-1}$. Given this, we see it likely that that these systems are tracing a multiphase medium where hot and cold gas is mixing at the interface between the CGM and IGM. We discuss this in detail in Section 5.3.

(ix) We have also identified 5 Si II, 10 Al II, 12 Fe II, 1 C II, 7 Mg I, and 1 Ca II transitions associated with C IV, Si IV, and Mg II doublets. We compute the associated comoving mass density of each ion and present them in Table 6 and Fig. 19. We compare our values with the work of Lan & Fukugita (2017) and find that $\Omega_{\rm Si\,II}$, $\Omega_{\rm Fe\,II}$, $\Omega_{\rm Mg\,I}$, and $\Omega_{\rm Al\,II}$ exhibit a flat evolution from redshift 2 to 5. We find that $\Omega_{\rm Si\,II}$, $\Omega_{\rm C\,II}$, and $\Omega_{\rm Al\,II}$ decrease by several orders of magnitude. However, this evolution is due to the association of these systems with only *weak* Mg II systems beyond redshift 5 while they are mostly associated with *strong* Mg II systems below redshift 5. We discuss this in detail in Section 5.4.

We find that C IV systems with $\log N_{\rm (sys)} > 14$ are preferentially physically associated with low-ionization systems and are likely to trace multiphase gas. Further MUSE (Bacon et al. 2010) observations of these absorbers will be able to identify the physical environment and galaxies responsible for the enrichment and their local contribution to the ionization field. Recent work by Fumagalli et al. (2017) has connected similar absorber pairs to clustered galaxy formation in filamentary structure at $z \simeq 3.22$. Extending this work to $z \simeq 5$ provides an exciting opportunity to explore the connection between absorption systems and the associated emission properties of the galaxies responsible for the metal pollution.

ACKNOWLEDGEMENTS

We thank Glenn Kacprzak, Michael Murphy, Nikki Nielsen, Stephanie Pointon, Adam Stevens, and the anonymous referee for useful discussions and Manodeep Singa for his expertise with code optimization. This work is based on observations made with the ESO telescopes at the La Silla Paranal Observatory under programme ID 084.A-0390(A). Parts of this research have made use of the Matplotlib library (Hunter 2007). ERW and AC acknowledge the *Australian Research Council* for *Discovery Project* grant DP1095600, which supported this work. AC is also supported by a Swinburne University Postgraduate Research Award (SUPRA) scholarship. Parts of this research were conducted by the Australian Research Council Centre of Excellence for All-sky Astrophysics (CAASTRO), through project number CE110001020.

REFERENCES

Adelberger K. L., Shapley A. E., Steidel C. C., Pettini M., Erb D. K., Reddy N. A., 2005, ApJ, 629, 636
Aguirre A., Schaye J., Kim T.-S., Theuns T., Rauch M., Sargent W. L. W., 2004, ApJ, 602, 38
Atek H. et al., 2015, ApJ, 800, 18
Bacon R. et al., 2010, in McLean I. S., Ramsay S. K., Takami H., eds, Proc. SPIE Conf. Ser. Vol. 7735, Ground-based and Airborne Instrumentation for Astronomy III. SPIE, Bellingham, p.773508
Becker G. D., Sargent W. L. W., Rauch M., Simcoe R. A., 2006, ApJ, 640, 69
Becker G. D., Rauch M., Sargent W. L. W., 2009, ApJ, 698, 1010
Becker G. D., Sargent W. L. W., Rauch M., Calverley A. P., 2011, ApJ, 735, 93
Becker G. D., Sargent W. L. W., Rauch M., Carswell R. F., 2012, ApJ, 744, 91
Becker G. D., Bolton J. S., Lidz A., 2015a, PASA, 32, e045
Becker G. D., Bolton J. S., Madau P., Pettini M., Ryan-Weber E. V., Venemans B. P., 2015b, MNRAS, 447, 3402
Boksenberg A., Sargent W. L. W., 2015, ApJS, 218, 7 (B15)
Bosman S. E. I., Becker G. D., Haehnelt M. G., Hewett P. C., McMahon R. G., Mortlock D. J., Simpson C., Venemans B. P., 2017, MNRAS, 470, 1919, (B17)
Bouwens R. J. et al., 2015, ApJ, 803, 34
Bouwens R. J., Illingworth G. D., Oesch P. A., Atek H., Lam D., Stefanon M., 2017, ApJ, 843, 41
Burchett J. N. et al., 2016, ApJ, 832, 124
Cai Z., Fan X., Dave R., Finlator K., Oppenheimer B., 2017, ApJ, 849, L18
Carswell R. F., Webb J. K., 2014, Astrophysics Source Code Library, record ascl:1408.015
Carswell R. F., Webb J. K., Cooke A. J., Irwin M. J., 2014, Astrophysics Source Code Library, record ascl:1408.017
Cen R., Chisari N. E., 2011, ApJ, 731, 11
Chabrier G., 2003, PASP, 115, 763
Chen S.-F. S. et al., 2017, ApJ, 850, 188

Churchill C. W., Trujillo-Gomez S., Nielsen N. M., Kacprzak G. G., 2013, ApJ, 779, 87
Codoreanu A., Ryan-Weber E. V., Crighton N. H. M., Becker G., Pettini M., Madau P., Venemans B., 2017, MNRAS, 472, 1023 (C17)
D'Odorico V. et al., 2013, MNRAS, 435, 1198 (D13)
D'Odorico V. et al., 2016, MNRAS, 463, 2690
Díaz C. G., Ryan-Weber E. V., Codoreanu A., Pettini M., Madau P., 2016, Boletin de la Asociacion Argentina de Astronomia La Plata Argentina, 58, 54
Doughty C., Finlator K., Oppenheimer B. D., Davé R., Zackrisson E., 2018, MNRAS, 475, 4717
Faber S. M., Jackson R. E., 1976, ApJ, 204, 668
Ferrara A., Pettini M., Shchekinov Y., 2000, MNRAS, 319, 539
Finlator K., Thompson R., Huang S., Davé R., Zackrisson E., Oppenheimer B. D., 2015, MNRAS, 447, 2526
Finlator K., Oppenheimer B. D., Davé R., Zackrisson E., Thompson R., Huang S., 2016, MNRAS, 459, 2299
Fumagalli M. et al., 2017, MNRAS, 471, 3686
García L. A., Tescari E., Ryan-Weber E. V., Wyithe J. S. B., 2017, MNRAS, 470, 2494 (G17)
Gauthier J.-R., 2013, MNRAS, 432, 1444
Haardt F., Madau P., 2012, ApJ, 746, 125 (HM12)
Heger A., Woosley S. E., 2002, ApJ, 567, 532
Hosokawa T., Yoshida N., Omukai K., Yorke H. W., 2012, ApJ, 760, L37
Hunter J. D., 2007, Comput. Sci. Eng., 9, 90
Kacprzak G. G., Churchill C. W., 2011, ApJ, 743, L34
Kacprzak G. G., Churchill C. W., Barton E. J., Cooke J., 2011, ApJ, 733, 105
Kacprzak G. G., Churchill C. W., Nielsen N. M., 2012, ApJ, 760, L7
Kacprzak G. G., Cooke J., Churchill C. W., Ryan-Weber E. V., Nielsen N. M., 2013, ApJ, 777, L11
Keating L. C., Puchwein E., Haehnelt M. G., Bird S., Bolton J. S., 2016, MNRAS, 461, 606
Kroupa P., 2001, MNRAS, 322, 231
Lan T.-W., Fukugita M., 2017, ApJ, 600, L1 (LF17)
Livermore R. C., Finkelstein S. L., Lotz J. M., 2017, ApJ, 835, 113
Madau P., Dickinson M., 2014, ARA&A, 52, 415
Madau P., Ferrara A., Rees M. J., 2001, ApJ, 555, 92
Maio U., Ciardi B., Dolag K., Tornatore L., Khochfar S., 2010, MNRAS, 407, 1003
Mason C. A., Trenti M., Treu T., 2015, ApJ, 813, 21
Matejek M. S., Simcoe R. A., 2012, ApJ, 761, 112
Morton D. C., 2003, ApJS, 149, 205
Nestor D. B., Johnson B. D., Wild V., Ménard B., Turnshek D. A., Rao S., Pettini M., 2011, MNRAS, 412, 1559
Nielsen N. M., Churchill C. W., Kacprzak G. G., Murphy M. T., 2013a, ApJ, 776, 114
Nielsen N. M., Churchill C. W., Kacprzak G. G., 2013b, ApJ, 776, 115
Nielsen N. M., Churchill C. W., Kacprzak G. G., Murphy M. T., Evans J. L., 2015, ApJ, 812, 83
Nielsen N. M., Churchill C. W., Kacprzak G. G., Murphy M. T., Evans J. L., 2016, ApJ, 818, 171
Oppenheimer B. D., Davé R., 2006, MNRAS, 373, 1265
Oppenheimer B. D., Davé R., Finlator K., 2009, MNRAS, 396, 729
Oppenheimer B. D., Schaye J., Crain R. A., Werk J. K., Richings A. J., 2018, MNRAS, 481, 835
Pallottini A., Ferrara A., Gallerani S., Salvadori S., D'Odorico V., 2014, MNRAS, 440, 2498
Pettini M., Madau P., Bolte M., Prochaska J. X., Ellison S. L., Fan X., 2003, ApJ, 594, 695
Planck Collaboration et al., 2015, A&A, 582, A31
Prochaska J. X., Chen H.-W., Wolfe A. M., Dessauges-Zavadsky M., Bloom J. S., 2008, ApJ, 672, 59
Robertson B. E. et al., 2013, ApJ, 768, 71
Ryan-Weber E. V., Pettini M., Madau P., 2006, MNRAS, 371, L78
Ryan-Weber E. V., Pettini M., Madau P., Zych B. J., 2009, MNRAS, 395, 1476
Salpeter E. E., 1955, ApJ, 121, 161
Schaye J., Aguirre A., Kim T.-S., Theuns T., Rauch M., Sargent W. L. W., 2003, ApJ, 596, 768
Schaye J., Carswell R. F., Kim T.-S., 2007, MNRAS, 379, 1169
Simcoe R. A. et al., 2011, ApJ, 743, 21 (S11)
Simcoe R. A., 2006, ApJ, 653, 977
Songaila A., 2001, ApJ, 561, L153
Songaila A., 2005, AJ, 130, 1996 (S05)
Steidel C. C., Erb D. K., Shapley A. E., Pettini M., Reddy N., Bogosavljević M., Rudie G. C., Rakic O., 2010, ApJ, 717, 289
Turner M. L., Schaye J., Steidel C. C., Rudie G. C., Strom A. L., 2014, MNRAS, 445, 794
Yoshida N., Omukai K., Hernquist L., Abel T., 2006, ApJ, 652, 6
Zou S., Petitjean P., Noterdaeme P., Ledoux C., Krogager J.-K., Fathivavsari H., Srianand R., López S., 2018, AA, 616, A158

SUPPORTING INFORMATION

Supplementary data are available at *MNRAS* online.

online_appendix_final.pdf

Please note: Oxford University Press is not responsible for the content or functionality of any supporting materials supplied by the authors. Any queries (other than missing material) should be directed to the corresponding author for the article.

This paper has been typeset from a TEX/LATEX file prepared by the author.